# Title: Ultrafast electronic and vibrational spectroscopy of electrochemical transformations on a metal-oxide surface during oxygen evolution from water

**Authors:** Tanja Cuk[1,2,3*], Xihan Chen[4], Suryansh Singh[2,3], Michael Paolino[5], James Stewart[1], and Ilya Vinogradov[2]

**Affiliations**:

[1]Department of Chemistry, University of Colorado, Boulder, Boulder, 80303

[2]Renewable and Sustainable Energy Institute (RASEI), University of Colorado, Boulder, Boulder, 80303

[3]Materials Science and Engineering Program, University of Colorado, Boulder, Boulder, 80303

[4]Department of Mechanical Engineering, Southern University of Science and Technology, Shenzhen, Guangdong Province, China 518055

[*]Corresponding Authors: tanja.cuk@colorado.edu

**Abstract:** The oxygen evolution reaction (OER) from water fuels the planet through photosynthesis and is a primary means for hydrogen storage in energy technologies. Yet the detection of intermediates of OER central to the catalytic mechanism has been an ongoing challenge. This review covers the relevance of ultrafast electronic and vibrational spectroscopy of the electrochemical transformations of a metal-oxide surface undergoing OER. The electron doped $SrTiO_3$/electrolyte is the system under review because of its high photocurrent efficiency with an ultrafast light trigger and because it allowed for detection of intermediate forms across the electromagnetic spectrum. The first part covers how the efficient catalytic reaction is triggered by ultrafast light pulses, describing the Schottky diode, the depletion layer, and Helmholtz layer under operating conditions to the extent possible. The second part covers the detection of the surface bound intermediates by transient spectroscopy. These target ultrafast (ps-ns) electron transfer from (or hole-trapping to) bound surface water species that are associated with the reactive oxygen intermediates of OER (e.g. $OH^*$, $O^*$). Their detection via a broadband visible probe, a mid-infrared evanescent wave, and coherent acoustic waves is then described. These target, respectively, the electronic states, the vibrational levels, and the lattice strain associated with the intermediates. The review is primarily concerned with how the measurements are made and the intermediates' experimental spectra. The theoretical descriptions are brought in as a needed to provide context to spectra that are difficult to interpret on their own. A concluding section summarizes the essential findings and methodologies.

## Table of Contents:

## I. Introduction

Chemical transformations have far-reaching impacts for energy utilization, energy storage, and chemical synthesis. The understanding of how chemical transformations occur in real, complex environments is fundamental to our ability to control them and scale them for our needs. Further, at these complex interfaces, chemical transformations occur in a markedly efficient and directed manner and are therefore catalytic or occur with underpinnings which are understandable and tunable. Yet, while mechanistic pathways of catalysis have been proposed for decades, our ability to follow them directly and along the axis which best defines their trajectory—time—has been limited.

Catalytic reactions are described by a set of meta-stable intermediate chemical forms that reorganize reactants into products. On the other hand, the activity of material surfaces for catalysis has been differentiated largely by their cumulative product evolution[1]. This leads to a dichotomy between experiment and theory in the field of catalysis, motivated by what can be practically defined from either end. For example, a material's activity, measured experimentally, is plotted as a function of a largely theoretical descriptor, with the most general being the free energy difference(s) between intermediate chemical forms[2].

Different methodologies have been applied previously to try and isolate and detect reaction intermediates as a function of time and to relate the experimental and theoretical axes causally, especially in regards to homogeneous catalysis[3], where reactions have been halted at points within the catalytic cycle by potential, light, or changing reactant flows. A major step beyond this would be to directly time-resolve the reaction steps, obtain their rates of forward and back transfer, and follow meta-stable populations. Such experiments would provide both kinetic and thermodynamic quantities by which to tailor the material and its environment for desired functionality, such as the selectivity and speed of product evolution[4].

To be able to time-resolve a catalytic cycle for its reaction steps, there are at a minimum three critical considerations. One is that the cycle should be triggered at a distinct time-point and that the trigger should initiate a fully spontaneous (*e.g.* downhill) reaction. The spontaneous reaction means that the catalysis proceeds through sequential steps, such that each meta-stable intermediate occurs with a separate potential energy minimum (Figure 1) that describes its bonding environment, and one occurs after another. In this regard, a time-axis exists that tracks the spatial coordinate of the potential energy surface (PES). The distinct time-point is necessary such that the "birth" of each intermediate is captured and separated from intermediates occurring before and after. Ideally, an ultrafast trigger of the reaction is utilized since charge-trapping at material interfaces can occur in less than a picosecond.

Second, the spectroscopic probe of the bonding environment should be sufficiently time-resolved, multi-modal, and surface-sensitive. Sufficient time resolution allows one to collect time-traces that resolve sequential kinetics. Multiple modalities are required to obtain information on both vibrational normal modes and the electronic states of the intermediates. A vibrational spectroscopy targets the shape of the PES bounding the intermediate, while an electronic spectroscopy targets its minimum. Here, the electronic spectroscopy is within the ultraviolet-visible range and the vibrational spectroscopy is within the mid-to-far infrared. While infrared spectroscopy readily defines the intermediates molecularly, the visible spectroscopy encompasses a broader set of intermediates—independent of a particular geometry—whose populations lead to kinetic events. This dichotomy is important since not one distinct geometry will necessarily lead to bond formation events[5-6]. Finally, it is important that the probe is surface sensitive, and this is achieved in the most facile fashion using optical reflectance techniques—a simple reflectance of a UV-visible probe and the utilization of an evanescent wave in the mid-infrared regime. There are certainly non-linear optical probes now available to get more surface sensitive, of which second harmonic and sum frequency generation are the most well-known. However, these do net yet investigate a spontaneous, downhill chemical reaction in time.

Third, it is important to apply appropriate phenomenological analyses to the spectral and kinetic data. The purpose of these analyses is two-fold: 1) Resolve the intermediate's "bare" spectral signatures from a complex, condensed-phase environment and from other species present at the interface, and 2) Connect the observed spectra and kinetics of the reaction intermediates to the reaction conditions controlled by the experimentalist. These phenomenological analyses, which include principal component analyses and mode coupling to the environment will be mentioned as they arise in the data. The mathematical foundation for these analyses that connects them to the observables has been reviewed elsewhere[7].

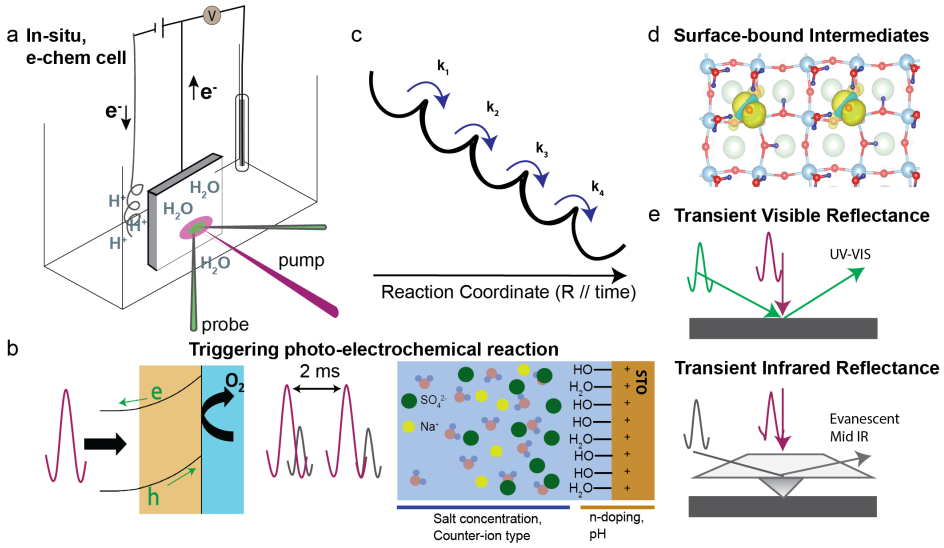


**Figure 1: Overview of transient optical spectroscopy of a chemical reaction at a surface.** a) *In-situ* electrochemical cell for transient spectroscopy, b) Triggering electrochemistry using n-type semiconductor/aqueous interface to separate charge with ultrafast band-gap excitation. Interface is modulated by pH, n-doping, and counter-ion concentrations, c) Fully spontaneous reaction with four meta-stable intermediates d) Detection of surface bound intermediates, Ti-OH*, by optical and vibrational transitions, and e) Techniques include transient optical reflectance, transient attenuated total reflection-IR (ATR).

One of the model systems for

time-resolving catalysis at solid-liquid interfaces is the n-type semiconductor/aqueous interface for the oxygen evolution reaction (OER) from water (Figure 1 a, b). While a target of *in-situ* investigations by pump-probe spectroscopy[8], x-ray[9-11], and microscopy[12-13], resolving the catalytic cycle through bond-formation as a series of distinct and tunable reaction steps has not yet been achieved. On the other hand, these works and that of a model surface which is the focus of this review, electron doped or n-type $SrTiO_3$ (hereafter, n-STO), do suggest that quantification and modulation of the causal sequence of reaction steps is achievable.

The OER reaction from water is a canonical one to time-resolve in that it involves multi-electron and proton transfer steps, chemical bond-formation events (e.g. the O-O bond), and is highly selective for its product. This allows the spectroscopy to target multiple steps inclusive of a bond formation event all leading to the same final product. Furthermore, it is the reaction that powers plant photosynthesis which stores sunlight energy in chemical form. In Photosystem II, which is arguably is the fastest at oxidizing water, the water oxidation complex has been well-characterized for each of the four added charges prior to $O_2$. Yet, how these multi-electron transfer steps reorganize chemical bonds of water into $O_2$ ($S_4 \rightarrow S_0$) is an open challenge. Material and molecular systems provide a platform for synchronizing these chemical events with a laser pulse. For the OER reaction, a simplified single site mechanism includes electron and proton transfers between $H_2O/OH^*$ ($\Delta G_{OH*}$), $OH^*/O^*$ ($\Delta G_{O*}$), $O^*/O\text{-}O^*$ ($\Delta G_{O\text{-}O*}$), and $O\text{-}O^*/O_2$ ($\Delta G_{O2}$). Figure 1c shows a PES of four meta-stable intermediate populations prior to $O_2$ evolution, which are a result of either electron transfer or a dark chemical step and encompass a range of proton configurations. Figure 1d shows these intermediates as a coverage of electron deficient oxygen on the surface.

The ultrafast excitation and efficient charge separation at a well-defined n-semiconductor/aqueous interface enables triggering OER at a distinct time point, from which the subsequently downhill and sequential reaction steps can be followed by optical (absorption, emission) and vibrational (attenuated total reflection (ATR)-IR) spectroscopies (Fig. 1e). The entirety of the chapter concerns the model, STO system, and is organized as follows: Part II (*Photo-triggering an efficient catalytic reaction by ultrafast light pulses*) addresses the paradigm of the semi-conductor/aqueous interface and how to trigger the photo-electrochemical reaction with an ultrafast light pulse from a well-characterized interface. Part III (*Detecting surface-bound intermediates by transient spectroscopy*) addresses how to resolve spectral signatures of the surface-bound intermediates by time-resolved optical probes from the visible to the mid-infrared using reflective geometries. Coherent acoustic waves also detected by a visible probe further the observables to the GHz regime of acoustic phonons.

STO is a $d^0$ compound, such that: 1) the ground state has little background excitations, since the O 2p bonding orbitals are filled and the 3d anti-bonding orbitals are empty, and 2) electron-transfers out of the bonds come from the O 2p bonding orbitals, rather than 3d orbitals which exhibit complex electron-electron repulsions. Therefore, the model system is likely one of the simplest of the transition metal oxides on which to time-resolve the OER reaction. Other model systems in terms of electronic structure include the rutile and anatase $TiO_2$. These are a target of future studies, although their crystal structures are substantially more complex than STO, a centrosymmetric perovskite. The methodologies presented on the STO/electrolyte interface

should be applied to other materials to both test the interpretations forwarded here and to truly design solar-to-fuel systems around the reaction steps of catalysis.

## II. Photo-triggering an efficient catalytic reaction by ultrafast light pulses:

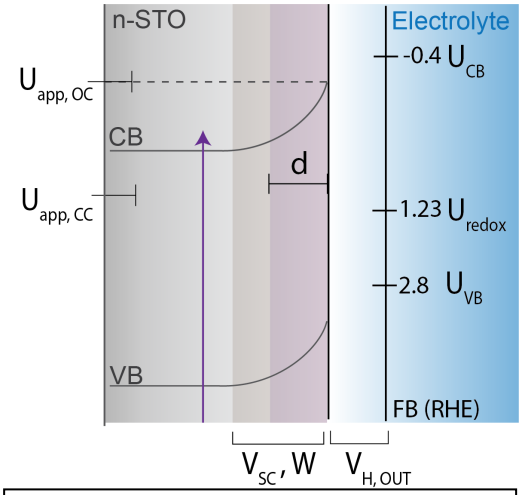


**Figure 2**: n-STO/electrolyte interface. $U_{app,OC}$ , $U_{app,CC}$ refers to the potential at the back of the electrode under open, closed circuit conditions during photo-excitation. $V_{SC}$, W, and d refer to the voltage drop across the diode in the semi-conductor, its depletion width, and the adsorption depth of the above band-gap light excitation. $V_{H,OUT}$ refers to the voltage drop across the Helmholtz layer of free ions. The potentials of the conduction, $U_{CB}$, and valence, $U_{VB}$ bands are shown for flatband (FB) conditions on the RHE scale.

To trigger of OER at an ultrafast timescale, a Schottky diode is photo excited. The Schottky diode naturally occurs at the n-type semiconductor-electrolyte interface due to the equilibration of the chemical potential of the electrons in the semiconductor with that of reactants in the electrolyte. At aqueous interfaces for which ions in the electrolyte or adsorbed on the surface cannot be reduced or oxidized, the relevant reaction that levels the chemical potential across the interface is the $O_2/H_2O$ oxidation-reduction reaction. The resulting electric field in the semiconductor can then be used to separate photoexcited electron-hole pairs, such that the valence band (VB) holes accumulate at the interface and evolve $O_2$ from water. A depiction of this Schottky diode and the level alignment at the aqueous interface is shown in Figure 2. The following is divided into three sections that characterize this interface for ultrafast light excitation of a steady-state catalytic reaction: The Schottky diode at the n-STO/electrolyte interface (A), The depletion and Helmholtz layers at the n-STO/electrolyte interface, and (C) Defining the OER surface for transient spectroscopy. Part II A and Part II B summarize original work cited by ref.[14] Part II C summarizes original work cited by ref. [15-16]

### A. The Schottky diode at the n-STO/electrolyte interface:

Here, the photoexcitation of the diode created at the n-STO/electrolyte interface with an applied bias is detailed first using standard solid-state diode equations. In the next section, the interfacial capacitances associated with both the electric field within the semiconductor and the electrolyte (termed the Helmholtz layer) are discussed with a simplified circuit diagram for an ideal n-type semiconductor/water interface.

The Schottky diode at the n-STO/electrolyte interface is a model system for studying the kinetics of $O_2$ evolution from water by transient spectroscopy[14]. Figure 3a shows the results of steady-state current measurements with n-STO (0.1 wt. % Nb) as the photoanode and with 500 Hz, 150 fs laser, ultraviolet (266 nm or 300 nm) excitation. The voltage is applied on the back of the STO sample. The reference electrode for the 3-electrode cell is Ag/AgCl. Both this reference and the reversible hydrogen electrode (RHE) will be used in the discussion that follows. yttttttFor STO, as will be detailed below, the conduction band (CB) is at -0.4 V vs. RHE and the valence

band (VB) is at 2.8 V vs. RHE. Therefore, like many wide-band gap n-type semiconductors, the electrons and holes straddle the $O_2/H_2O$ potential at 1.23 V vs. RHE.

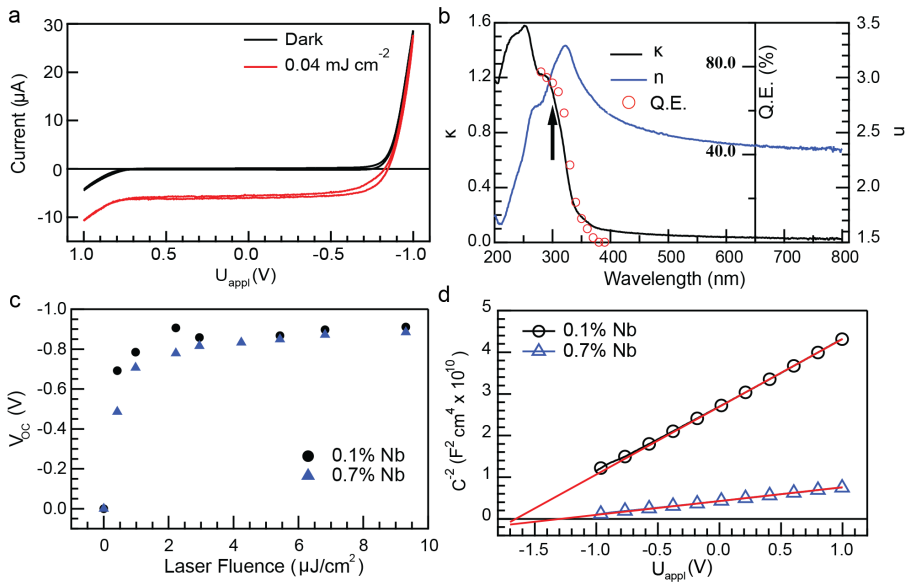


**Figure 3**: Photo-electrochemical response of n-STO/electrolyte interface at pH 13 vs. a Ag/AgCl reference electrode. a) Current-voltammogram in the dark and under light excitation, b) real (n) and imaginary (k) indices of refraction for n-STO. Quantum efficiency of light excitation increases according to k c) Photovoltage at open-ciruit ($V_{OC}$) for 0.1% Nb and 0.7% Nb STO samples as a function of laser fluence, d) Mott-Schottky plots of the inverse squared capacitance for 0.1% and 0.7% Nb STO. All taken with kHz laser excitation (300 nm, 0.04 mJ/cm$^2$) except for the Q.E. in b) taken with the monochromated output of a Xenon lamp.

The cyclic voltammogram, or the measured current while sweeping the voltage is shown in Fig. 3a in the dark and under light excitation. The interface exhibits an ideal diode like behavior under photoexcitation. For cathodic voltages more negative than −0.85 V vs. Ag/AgCl the n-type semiconductor is in a forward bias regime where the surface electric field that separates the electron−hole pairs (depletion layer) decreases in width until there is no longer any photo-current. Under anodic voltages, the semiconductor is largely in a reverse-bias regime where the width of the depletion layer is maximized, and the anodic current is potential-independent. Both the shape of this curve and the quantum efficiency of the photocurrent (>75%)[14], defined as the ratio of the photocurrent to the absorbed light flux, are similar to that obtained with a continuous xenon lamp source. The high quantum efficiency is achieved by ensuring that the excitation absorption depth is smaller than or equal to the width of the depletion layer. The excitation absorption depth is approximated by $d = \lambda/4\pi k$, where $\lambda$ is the excitation wavelength and k is the imaginary part of the refractive index. As shown in Figure 3b, where the quantum efficiency is plotted together with the index of refraction as a function of wavelength, the quantum efficiency closely follows k.

We can quantify these statements by using the Schottky approximation for the n-type semiconductor/liquid interface. Within the Schottky approximation, the depletion width W (Figure 2) is given by the n-p junction equations according to:

$$W = \sqrt{\frac{2\epsilon\epsilon_0}{e_0 N_d}\left|V_{SC} - \frac{k_B T}{e_0}\right|} \qquad (1)$$

where $N_d$, $\epsilon, \epsilon_0$ $e_0$, $k_B$, and T represent the doping density, the dielectric constant of the semiconductor, the vacuum permittivity, the electronic charge, the Boltzmann constant, and the

absolute temperature, respectively. $V_{SC}$, the built-in voltage in the semiconductor, is the potential difference across the diode in the semiconductor when the chemical potential of the electrons and the redox reaction equilibrate. The potential differences are reported as back to front faces of the semiconductor with respect to the electrolyte. For the Schottky equation under bias, $V_{SC}$ is replaced by $V + V_{SC}$. Thus, $-V_{SC}$ needs to be applied to "flatten" the bands such that there is a negligible voltage drop and depletion width in the semiconductor. $V_{SC}$ can be measured by shining light on the diode at open circuit for which no leads are attached such that electrons are shuttled to the back of the sample and holes to the front. Figure 3c reports this open circuit photovoltage ($V_{OC}$) as a function of light fluence. The value saturates at -0.85 V at low fluence and close to the onset of the anodic photocurrent in Figure 3a.

Given the nominal doping density of STO, 0.1 wt. % Nb, and the measured $V_{SC}$, or 0.85 V, W= 25 nm. One can then compare the depletion width to the excitation absorption depth, which for 266 nm excitation is $d = \lambda/4\pi k$ = 17 nm. Indeed, the Schottky diode has a high QE for charge-separation when d is significantly less than W. To relate the built-in ($V_{SC}$) and applied (V) voltages to relevant circuit potentials denoted by U ($U_{app}$ of the working electrode, $U_{REDOX}$ of the $H_2O/O_2$ reaction, and $U_{FB}$ of the semiconductor Fermi level), one needs to consider a non-ideal diode in which a Helmholtz screening layer exists. We get to this below. However, in both instances $V_{OC}$ measures the built-in voltage in the semiconductor, $V_{SC}$.

| **Table I** | **n-$SrTiO_3$ (Nb 0.1%)** |
|---|---|
| Band Gap | 3.15 eV |
| Pump Excitation | 4.66 eV (266 nm) |
| Absorption Depth (d) | 17 nm (266 nm) |
| Depletion Width (W) | 25 nm |
| Built-in Voltage ($V_{SC}$) | 0.85 V |
| Positive charge in W | 2 x $10^{13}$ $cm^{-2}$ ($N_dW$) |
| Flatband potential ($U_{FB}$) of semiconductor | -0.5 vs. RHE<br>-1.5 V vs. Ag/AgCl at pH 13 |
| Valence Band ($U_{VB}$) | 2.8 V vs. RHE |
| Conduction Band ($U_{CB}$) | -0.4 V vs. RHE |
| Doping Density ($N_d$) | 8 x $10^{18}$ $cm^{-3}$ |
| Excitation Fluence | 0.04 $mJ/cm^2$ |
| Hole Fluence (75% QE) | 4 x $10^{13}$ $cm^{-2}$ (2% of $S_0$) |
| Excitation area | 5*$10^{-4}$ $cm^2$ |
| Turnover rate | 1 $O_2$/site-sec |

Table 1 shows the relevant diode parameters for photo-induced charge separation at the n-STO/electrolyte interface used most routinely: the STO bandgap, the usual excitation wavelength, the excitation absorption depth, depletion width, and the built-in voltage. The charge/$cm^2$ needed to equilibrate the chemical potential across the interface is given by $N_dW$ (2 x $10^{13}cm^{-2}$). This charge density is an order of magnitude higher than the fluence at which the photovoltage (Figure 3c) saturates (2 $\mu J/cm^2$ = 2 x $10^{12}$ $cm^{-2}$); this is anticipated since electrons travel to the back of the electrode during photo-excitation (a width of 0.5 mm), which means a much smaller capacitance than that of the depletion layer (25 nm) is utilized to level the potential across the bulk of the sample. The capacitances are treated as parallel plate capacitors, both for the built-in voltage across the depletion layer and for the photo-voltage drop across the full thickness of the semiconductor; more complex forms can be treated which consider diffusion lengths in addition to the sample depth[17].

Most of the review concerns the 0.1% Nb-doped $SrTiO_3$ samples described in this table. However, highly doped samples (0.7% wt. Nb) are utilized to ascertain the role of dopants and doping density. They have similar diode characteristics, albeit a smaller depletion width (9 nm) and somewhat lower quantum efficiency (~65%). Overall, the Nb-doping will efficiently dope the conduction band with electrons, which leads to the regular Schottky behavior. This is also evidenced by the uniform distribution of Nb-doping with a Nb(V) oxidation state[18], the conductivity[19], and Hall effect measurements[19].

## B. The Depletion and Helmholtz layers at the n-STO/aqueous interface

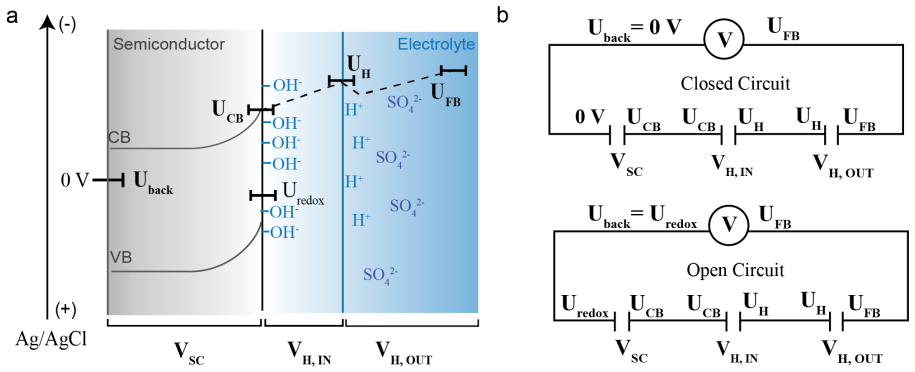


**Figure 4:** Inner and Outer Helmholtz Layers. a) Diagram of the interface, including the potential at the back of the electrode, $U_{back}$, potential at the edge of the bare semiconductor, $U_{CB}$, the potential at the end of the inner Helmholtz layer, $U_H$, and the flatband potential ($U_{FB}$). In the diagram, $U_{back}$ is at 0 V vs. Ag/AgCl for closed circuit. It becomes $U_{redox}$ for open circuit. b) Equivalent circuits for open and closed circuit where $V_{SC}$, $V_{H,IN}$, and $V_{H,OUT}$ denote voltage drops across the bare semiconductor, the inner Helmholtz layer, and the outer Helmholtz layer.

Next, the full interfacial energetics of the semiconductor-electrolyte interface are considered, which includes modeling of the potential distribution across both the depletion layer ($V_{SC}$) and the Helmholtz layer ($V_H$)[20-21]. The Helmholtz layer comes from free ions, adsorbed ions or molecules, new surface bonds with solution species, and oriented dipoles in the electrolyte that accumulate at the interface (Figure 4a). Here, we consider the two most prominent origins of this layer at the n-type semiconductor-electrolyte interface[20]. For the particular case of metal oxides and metal sulfides semiconductors, the inner Helmholtz layer ($V_{H,IN}$) derives from increasing the pH of the solution from the point of zero charge, which results in a pH dependent Fermi level as will be described in detail below.

The other, more general origin of the Helmholtz layer depicted in Figure 4a ($V_{H,OUT}$) are the free ions in the electrolyte needed to transport charge effectively (e.g. $SO_4^{2-}$, $H^+$, $OH^-$, $PO_4^{2-}$). These will accumulate at the interface to screen the charge in the electrode, which will be positive for the n-type semiconductor interface and anodic potentials. The capacitor model for the interface is given in Figure 4b and includes the capacitance of the "bare" semiconductor ($V_{SC}$ drops over $C_{SC}$) and the Helmholtz layer ( $V_H$ drops over $C_H$) in series. In the deGryse modelling[21] of the potential drop across the interface, $V_H$ is treated as arising from the free ions alone with no adsorption. The capacitance of the semiconductor is that of the space charge depletion layer, the capacitance of the Helmholtz layer is that of a parallel plate, and the total charge across the Helmholtz layer is equal to that of the depletion layer. This modelling leads directly to the Mott-Schottky equation with a Helmholtz layer[21]. The total capacitance of the series capacitors ($1/C^2$) is related the Fermi level when the bands are flat and no depletion layer exists, or the flatband potential ($U_{FB}$). It is also related to the the doping density ($N_d$), and the Helmholtz capacitance ($C_H$) by:

$$\frac{1}{C^2} = \frac{1}{C_H^2}\left[1 + \frac{2C_H^2}{q\varepsilon N_d}\left(U - U_{FB} - \frac{kT}{q}\right)\right] \qquad (2)$$

U is the potential applied to the back of the semiconductor. An example Mott-Schottky plot for the n-STO/aqueous interface is shown in Figure 3d and the values obtained from the fitted equation are shown in Table I. These capacitance measurements are obtained from measuring the

current while sweeping the voltage and are traditionally done using alternating current. The doping density ($N_d$) is derived from the slope of $1/C^2$, while the flatband potential ($U_{FB}$) is from the intercept given a known Helmholtz capacitance, $C_H$. Commonly a $C_H$ of 20 μF/cm$^2$ is utilized for transition metal oxide semiconductors[14]. With this, $U_{FB}$ = -1.5 V vs. Ag/AgCl is obtained at pH 13, equivalent to -0.5 V vs. RHE, which is close to the value of the CB of STO (-0.4 V vs. RHE) reported in the literature[20]. With this CB edge, and the bandgap of STO, the VB edge will then be located at 2.8 V vs. RHE (Table I).

In the circuit diagrams, the potential drop across the ions alone is $V_{H,OUT}$ across $C_{H,\,OUT}$. Now we return to an "inner" Helmholtz layer with $V_{H,IN}$ across $C_{H,\,IN}$ arising from surface de-protonation[22]. A hydroxylated layer can also be understood as a parallel plate capacitor ($C_{H,\,IN}$): a layer of interfacial dipoles (*e.g.* M-OH$^-$) all pointing in the same direction across the planar interface. The same Mott-Schottky equation used above is also used to show that this inner, pH dependent Helmholtz layer exists. Namely, by applying the Mott-Schottky equation as a function of pH, a pH-dependent $U_{FB}$ is identified through a changing intercept. On high quality $TiO_2$ surfaces, a -59 mV/pH is found[23]. This shift is accounted for by the free energy of proton transfer to a bulk electrolyte[24]. It is also found for many mineral semiconductors[20], leading to the following definition of $U_{FB}$ at 25°C and 1 atm:

$$U_{FB} = U_{FB}^0 + 0.059V\left(pH_{pzc} - pH\right) \quad (2)$$

$U_{FB}^0$ is the flatband potential at point of zero charge for which no inner Helmholtz layer exits. It is important to note that the $N_dW$ charge in the depletion layer screened by the electrolyte is approximately ~$10^{13}$ cm$^{-2}$ whereas the surface site density of STO is ~$10^{15}$ cm$^{-2}$. Therefore, the charge associated with the interfacial dipolar hydroxylation could over-screen the charge in the semiconductor at higher pH which is then compensated by $H^+$ leading to the non-monotonic potential change in Fig. 4a[25]; importantly, the extent of over-screening depends on the amount and distribution of negative charge within the hydroxyl coverage of a surface. In the circuit diagrams, the free $H^+$ are grouped with the free counter-ions ($SO_4^{2-}$, $PO_4^{3-}$ , $OH^-$) in the outer Helmholtz layer.

Next, the interfacial energetics are modelled for two conditions utilized frequently in the experiments: open circuit, for which the electrode is allowed to equilibrate with the solution chemical potential and closed circuit, for which it is held at 0 V vs. Ag/AgCl[26]. The chemical potential of the solution is $U_{redox}$ of $H_2O/O_2$. The diode in the semiconductor will be divided into the "bare" semiconductor at the point of zero charge ($V_{SC}$), the inner Helmholtz layer ($V_{H,\,IN}$), and the outer Helmholtz layer ($V_{H,\,OUT}$). Both closed and open circuit conditions are modelled in the dark; this is the starting surface from which the photo-driven one is created. Further, for 0 V vs. Ag/AgCl, OER in the dark is not possible.

The equivalent circuits for the two conditions are modeled by parallel plate capacitors in series (Figure 4b). Applying Kirchhoff's law to the closed-circuit condition gives:

$$0\,V - U_{FB} = V_{SC} + V_{H,IN} + V_{H,OUT} \quad (4)$$

Here, the potential difference across the circuit is equal to $0\text{ V} - U_{FB}$ with 0 V vs. Ag/AgCl the voltage on the working electrode. Since $U_{FB}$ scales with -59 mV/pH due to the interfacial dipole, there is an increase in the potential difference with pH. This pH-dependent potential can drop

across either $V_{H,IN}$ and $V_{H,\,OUT}$ depending on whether the deprotonation occurs at the surface or within a layer of the electrolyte. Often it is treated as occurring across $V_{H,\,IN}$ alone which then adds to the potential difference across the semiconductor side of the interface. In this case, in the Schottky equations $V_{SC} + V_{H,\,IN}$ replaces $V_{SC}$.

In open-circuit conditions, the floating potential at the back of the electrode equilibrates to $U_{redox}$. The voltage applied across the interface is that needed to equilibrate the chemical potential of the electrolyte to that of the semiconductor: $U_{redox} - U_{FB}$. Applying Kirchoff's law (Fig. 4b) gives:

$$U_{redox} - U_{FB} = V_{SC} + V_{H,IN} + V_{H,OUT} \quad (3)$$

Here, $U_{redox}$ of OER scales with -59 mV/pH because a proton transfers to the electrolyte for each electron transfer in the reaction[24]. Therefore, $U_{redox}$ and $U_{FB}$ change equivalently with pH if the surface deprotonates via full proton transfers to solution. The potential drop across the interface is then constant with pH and therefore, many semiconductors have similar activity for OER at higher pH despite an increasingly cathodic $U_{redox}$.[20] The cyclic voltammetry for n-STO is shown at pH 7 and pH 13 in Fig. 5a. The change in the onset of $U_{redox}$ is clear through the shift in the curves to more cathodic potentials at higher pH, which is graphed as a function of pH in Fig. 5b. The pH dependence of $U_{FB}$ can be measured by $V_{OC}$. Since $V_{OC}$ flattens the bands in the semiconductor, it measures the total $V_{SC} + V_{H,IN}$ if the hydroxylation changes indeed occur at the very interface. As shown in Figure 5b, $V_{OC}$ increases from -0.85 V at pH 13 to -0.5 V at pH 7, with a slope of -45 mV/pH which moves approximately in concert with $U_{redox}$. Given the circuit diagram, the pH dependence of $V_{SC} + V_{H,IN}$ is then presumed to be compensated by $V_{H,OUT}$. Finally, with $U_{REDOX} - U_{FB} = 1.73$ and the measured $V_{OC}$, one can then obtain $V_{H,OUT} = 0.88$ V at pH 13 which increases to $V_{H,OUT} = 1.23$ V at pH 7. The large $V_{H,OUT}$ means that when the electrode is not at the flatband potential, the semiconductor bands at the electrolyte interface are lower to allow for the potential drop, as cartooned in Fig. 4a and Fig. 2. This potential difference is compatible with a linear Mott-Schottky equation including a Helmholtz capacitance as developed by De Gryse with NiO in mind[21].

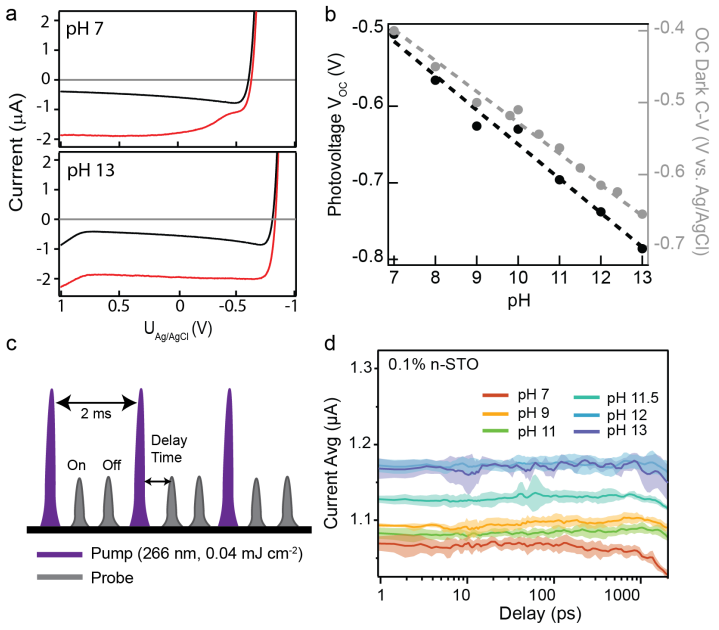


**Figure 5**: Steady state response of n-STO/electrolyte interface under kHz excitation and its pH dependence a) Cartoon of 500 Hz, 266 nm, 0.04 mJ cm$^{-2}$ light excitation used throughout the work. b) Cyclic voltammogram in the dark (black lines) and under light excitation (red lines) for pH 7 and pH 13, c) Photovoltage at open circuit (black dots) as a function of pH; the black dotted line is a linear fit with a slope of -45 mV/pH. Open circuit condition in the dark (gray dots) as a function of pH. d) The photocurrent at 0 V vs. Ag/AgCl during data taking with a probe and while scanning the sample, as a function of pH. The shaded areas define a standard deviation of less than 0.5%.

We have not determined the Helmholtz potential difference for the closed-circuit case, either in the dark or for light excitation. Since the Helmholtz drop is fairly large, it means that any change in potential at the back of the electrode will be distributed to an extent over the semiconductor and the free-ion Helmholtz layer[21]. Another complicating factor is photo-induced charge separation which leaves an accumulation of holes in the electrode and at the interface prior to transferring out during water oxidation. This can also change the balance of potential drops in the circuit, as has been reported in the past for the STO/electrolyte interface[14]. Therefore, in closed circuit, a common voltage is maintained at the back of the working electrode and a common intiates OER.

Finally, it is important to highlight that, unless stated, all the above measurements of photo-voltage and photo-current were done with the repetitive ultrafast excitation of the Schottky diode by above band gap photons depicted in Fig. 5c. It is a train of 400 fs, 266 nm pulses repeating at 500 Hz. Here, we report one final measurement which is the photocurrent as a function of acquisition time at closed circuit. The photocurrent obtained while scanning the sample leads to a constant current within 0.5% standard deviation in a single measurement, as shown in Fig. 5d[26]. The sample scanning methods that lead to this constant current are detailed next. The common fluence utilized is 0.04 mJ/cm$^2$ and is equivalent to 4 x $10^{13}$ charge-separated holes/cm$^2$ for a 75% Q.E (Table I). The charge separated holes/cm$^2$ translates to 2% surface excitation of surface oxygen sites on STO ($S_0$ = 2 x $10^{15}$ cm$^{-2}$). There can be 10% variation in the photo-current and quantum efficiency with pH; the specific dependence shown in Fig. 5d is detailed in the other review of the work[27].

In the rest of the review, OC refers to photo-exciting the sample at open circuit, for which there is no photocurrent. At OC, the electrode is allowed to equilibrate with the solution. When photo-excited, the electrons are shuttled to the back of the electrode but are prevented from leaving since they remain unconnected to the counter electrode that completes the reductive half-reaction. An epoxy is used to ensure that redox reactions do not occur at the back of the working electrode. CC refers to photo-exciting the sample at the closed-circuit condition with 0 V vs. Ag/AgCl at the back of the working electrode and the photocurrent shown in Fig. 5d.

## C. Defining the OER surface for transient spectroscopy:

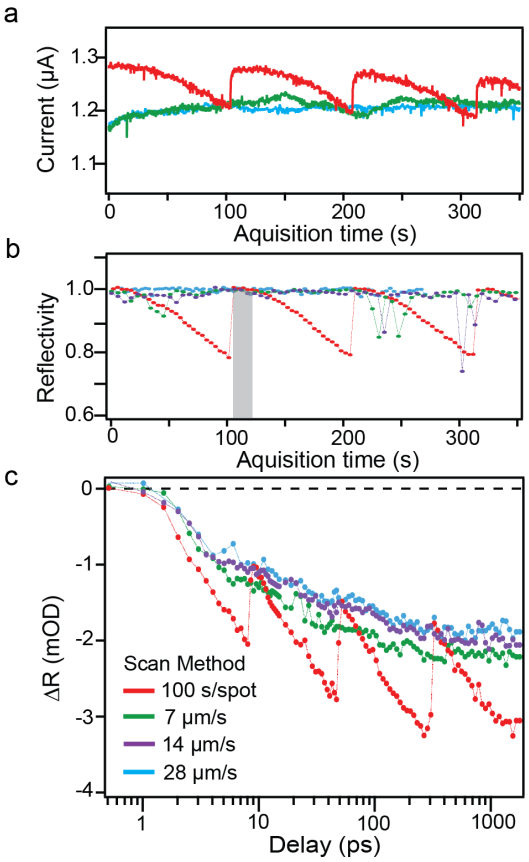


**Figure 6**: Photocurrent, ground state reflectance, and excited state reflectance for the static (red) and continuous (green, purple, blue) scan methods at pH 13. (a) Current passing through the electrode vs acquisition time. (b) Intensity of the broadband optical probe reflected from the sample vs acquisition time. (c) Kinetic trace of ΔR from the sample at 400 nm.

Since catalysts undergoing OER re-structure and the pump-probe technique averages over many pulses, it is important to find a methodology by which the initial state of the surface prior to excitation is recovered for each pulse—at least to the extent the probe in the pump-probe technique is sensitive to the initial state of the surface. Without this, there isn't a distinct time-point at which the catalytic reaction is triggered, and the re-structuring would affect the kinetics. In the following, the methodology chosen—a surface scan during data taking—is described first[15, 26]. Then, the surface characterization prior to[16], and post catalysis[15], is explained.

A sequence of ultrafast 266 nm, 500 Hz pump pulses arrive at the sample (Figure 5c). For each data point, there is both a time to acquire from many repetitive pump pulses on the sample (acquisition time) and a time difference between the pump and the optical probe (delay time). The sample is scanned (i.e. x-y-z stage motion) during acquisition and there are two methods: "static scan" and "continuous scan". In static scan, acquisition times are acquired over multiple spots on the sample that are separated by a fixed distance. Each spot is exposed to the 266 nm pump for a fixed amount of time (e.g. 100 seconds/spot or 50000 pump pulses within 100 s). In continuous scan, the sample stage is moved at a fixed rate (e.g. 7 μm/s or 28 μm/s) while all times are acquired sequentially.

Figure 6 reports on the sample degradation while the photocurrent evolves in a pH 13 electrolyte for the different scan methods. Continuous scanning results in a constant photocurrent, while the static scan method results in a decreasing photocurrent during each period (Figure 6a). The ground state reflectance monitored by a broad band white light probe remains constant for the continuous scan while it decreases for the static scan (Figure 6b). Given that the static scan involves a decreasing photo-current, the decrease in reflectance can be attributed to a roughened surface that scatters the visible probe, as described in detail in the full manuscript[15].

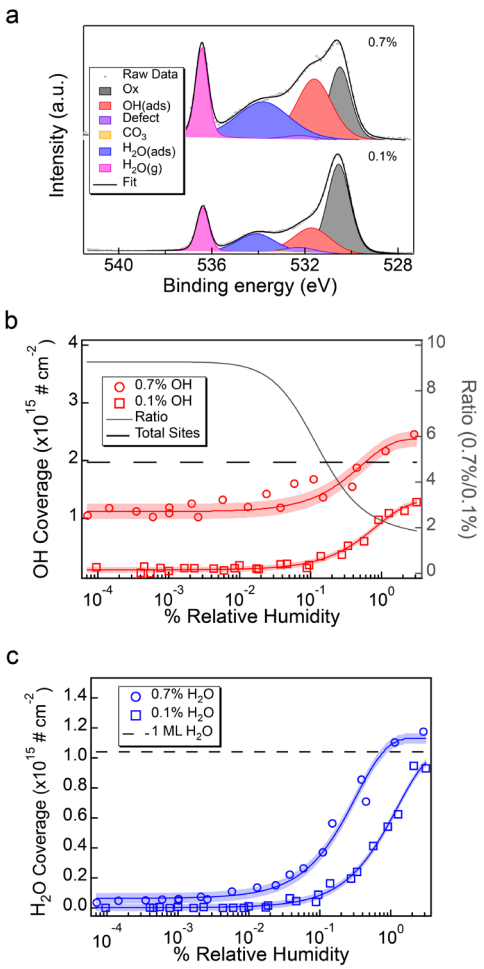


**Figure 7**: Ambient Pressure X-ray Photoelectron Spectroscopy for 0.1% Nb and 0.7% Nb STO a) O 1s spectra at 1% Relative Humidity (RH) from which –OH and $–OH_2$ coverages are derived, b) –OH coverage using a multilayer model applied to the raw data. Long, dashed line defines the number density of surface sites that support O on STO. c) $–OH_2$ coverage using a multilayer model applied to the raw data. Short, dashed line defines the number density of water in one monolayer. By 1% RH, a full hydration layer has already formed on both 0.1% and 0.7% Nb STO.

The excited state reflectance (ΔR) measured by pump-probe also changes while the photocurrent evolves and as a function of scan method. By continuously scanning at faster speeds, the acquisition time from a given surface area decreases and interestingly, the data converge to an unchanging ΔR (Figure 6c). This is shown by measuring ΔR for scan speeds from 7 μm/s (green trace) to 14 μm/s (purple trace) and finally to 28 um/s (blue trace). For the static scan of 100 s/spot (red trace), each time the pump moves to a clean surface, ΔR quickly jumps to the same value as ΔR for the 28 μm/s continuous scan, then gradually decreases as the acquisition time from the same sample spot increases, only to quickly jump back to the converged signal each time the pump is moved to a clean surface. Therefore, the ΔR from the 28 μm/s scan is identified as that of the nominally clean surface, with negligible contribution from the degradation. That the 28 um/s scan optically represents a nominally clean surface is also seen directly by optical microscopy[15].

Being able to take pump-probe delay points as arising from the same dark, equilibrated surface motivates the accurate characterization of that surface. One of the best ways to do so for a transition metal oxide in contact with water is ambient pressure x-ray photoelectron spectroscopy (AP-XPS). AP-XPS provides a unique opportunity to investigate the surface under increasing ambient relative humidity (RH), where the first hydration layer accrues on the surface from vacuum conditions[28-29]. While these experiments are conducted at neutral conditions and therefore are limited, they are specific enough for adsorbed water ($-OH_2$) and hydroxylated (-OH) sites to lend a molecular picture. In Figure 7a the data at 1% RH are shown for both 0.1% Nb and 0.7% Nb STO[16]; by 1 % RH, at least a full hydration layer has accrued. They are fit with cross-sections representing lattice oxygen, hydroxylated sites, adsorbed water, water vapor, and carbon contaminants. The full range of RH was analyzed using a multi-layer model and site coverages extracted from the integrated weights for each species. The coverage of hydroxylated and absorbed water sites is shown in Figure 7b and Figure 7c respectively for both 0.1% and 0.7% Nb STO. There is a clear change based on the doping density, with the 0.7% Nb STO reaching a fully hydroxylated layer by 1 % RH, and the

0.1% Nb STO only partially hydroxylated. For the data shown in this review, the focus is on the 0.1% Nb STO.

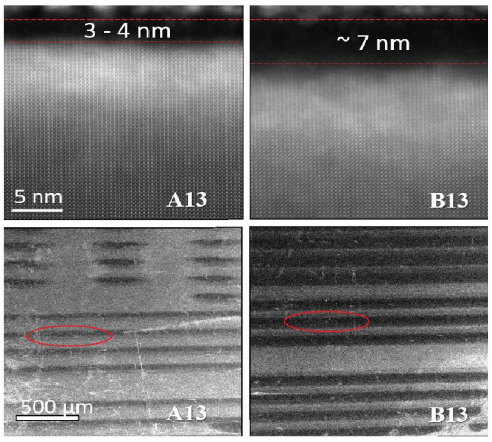


| Sample | A13 | B13 |
|---|---|---|
| TEM depth (nm) | 3-4 | 7 |
| SEM area ($mm^2$) | 0.024 | 0.035 |
| Charge passed ($x10^{-5}$ C) | 2.1 | 8.6 |
| # of O-atoms from sample/2 ($x10^{13}$) | 0.213 | 0.604 |
| $O_2$ from current ($x10^{13}$) | 3.28 | 13.4 |
| % Dissolution | 6.5 ± 3.0 | 4.5 ± 1.5 |

**Figure 8**: Electron microscopy post-catalysis at pH 13 (top) STEM images of the cross-sections of samples after 266 nm pump exposure for a 28 um/s scan (A13) and a 7 um/s scan (B13). The black band in the center shows the degradation depth contrasted against the bulk (crystal structure below lower dotted red line). (middle) SEM images for the same conditions showing the degraded surface area. The red oval marks on the SEM images show the place from where cross-sectional STEM specimens are prepared. Dark, oval spots on the sample surface result from static scanning, whereas continuous scanning produces evenly spaced lines. (bottom) Table estimating $O_2$ dissolution from the degraded STEM and SEM derived volume compared to the total $O_2$ evolution from the photo-excited current, as described in the text.

In the original manuscript, the suggestion is made that the change in the hydration layer is due to the increased basicity of sites that promotes proton dissociation for the higher doped STO. An effort was made to account for defects in the surface at ultrahigh vacuum that could also change the hydration layer. Atomic force microscopy shows a disordered surface with both $TiO_2$ and SrO exposed. X-ray Photoelectron Spectroscopy shows no measurable Ti(III) by the Ti 2p core-level and limits the Sr surface exposure to 30% from the Sr 3d core levels. The Nb dopants are uniformly distributed at the surface in a Nb(V) oxidation state by the Nb 3d core levels. Thus, Nb(V) replaces Ti(IV) to provide efficient electron donation to the conduction band. All of these statements reflect previous assessments of Nb-STO surfaces by vacuum science[30-32], and give a view of the starting surface for the optical spectroscopy.

The characterization techniques post-catalysis to understand the surface degradation are scanning electron microscopy (SEM) and cross-sectional scanning transmission electron microscopy (STEM). The cross-sectional sample was prepared by the in-situ lift-out method in a focused ion beam microscope. The STEM shows the depth with which the sample was degraded or re-constructed (Figure 8 top), while the SEM shows the aerial view of the surface degradation (Figure 8 middle). The aerial view well-depicts the scanning method during data acquisition: for continuous scans, even and continuous lines are observed, while for the static scan the degradation is confined to finite area spots. The aerial view and the depth are utilized to give an upper limit on how much of the sample dissolved into the electrolyte during catalysis.

By assuming that the dissolution process during oxidation involves at most two electron transfers per oxygen site, an upper limit of the current that evolves $O_2$ from the lattice of STO rather than $O_2$ from $H_2O$ can be obtained (Figure 8 table). This assumes a lattice oxygen evolution reaction (LOER) from STO, as detailed in the original publication. It is valid in the sense that STO is a noble metal compound, such that the metals are

both in oxidation states that cannot be further oxidized, e.g. Ti(IV) and Sr(II). Such a dissolution reaction is also suggested to be competitive with water oxidation on transition metal oxides by the relative reaction free energies[33]. The table reports the % dissolution for the 28 um/s scan, for which the degradation is not observed optically, and for the 7 um/s scan. Within error, these are the same and contribute on average to below 6% of the total current. The same is true whether employing a continuous or static scan, and for either 100 sec or an hour. Since the dissolution reaction is a constant percentage of the total current, independent on the method or time of acquisition, it was proposed that it is the dominant reaction thermodynamically allowed alongside OER. It is important to note that while this degradation occurs, since it constitutes an upper limit of 6% to the total current, only 6% of the holes separated by the electric field at the Schottky barrier and seen by the optical reflectance can contribute to the side reaction.

## III. Detecting surface-bound intermediates by transient spectroscopy

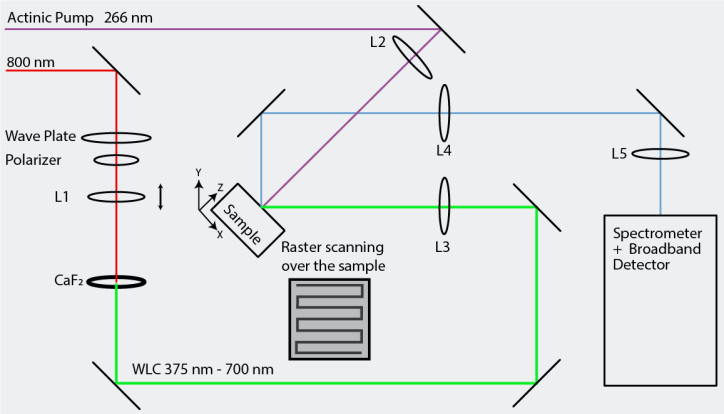


**Figure 9** Transient optical reflectance set up, including the pump that excites the catalysis (266 nm), the broad band probe (in the visible, 375-700 nm), and the spectrometer/broadband array detector. The reflectance geometry is shown along with the stage motion for raster scanning.

The methods of Part II to photo-trigger an efficient catalytic reaction by ultrafast light pulses are here combined with ultrafast optical spectroscopy in the visible[34] and mid-infrared ranges[35-36] to detect the surface-bound intermediates of the reaction. The transient, pump-probe setup is diagrammed in Figure 9. The setup contains the UV, band-gap pump excitation and the reflected probe (45°) from the working electrode of the electrochemical cell. For the visible range (as shown), the reflected probe is generated by $CaF_2$ to create broadband white light (375-700 nm) from the 800 nm, 150 fs Ti:Saphire beam. For the mid-infrared range, the probe is generated by an optical parametric amplifier tunable from the near IR to the 12 μm range with approximately 150 $cm^{-1}$ of bandwidth at each center wavelength, detectable by a 64-element array MgCdTe detector (32 elements are utilized for referencing). For the data reported below, the pump and probe are delayed by a mechanical delay stage through 4 ns. A transient reflectance with $R_{ON}$ after a pump pulse and $R_{OFF}$ at the same delay but with the pump pulse blocked (see Figure 5c for the probe sequence), is measured according to:

$$\Delta R = -\log\left(\frac{R_{ON} - R_{OFF}}{R_{OFF}}\right) \quad (5)$$

This formulation is the same for the mid-infrared and visible ranges. For the visible range, the sample is scanned, as described in Part II, using a motorized x-y stage cartooned in Fig. 9. For the mid-IR range, the data are mostly collected at open-circuit for which the clear degradation shown above is not observed. During closed circuit, the surface reconstruction is also not observed to

affect the mid-infrared probe. Finally, the photo-electrochemical cell used in the mid-infrared regime restricts the photocurrent; 1 M NaOH is required to achieve at most 50% quantum efficiency.

In the following, the free energies of the reaction steps at the photoexcited semiconductor-liquid interface are first briefly described (Part IIIA), which identifies what the transient spectroscopy aims to detect and situates the observables within the context of electrochemical reaction steps. Then, the visible (Part IIIB) and mid-infrared transitions (Part IIIC) of STO are discussed and associated with electronic states and normal modes of intermediates involved in OER. Finally, a coherent acoustic wave in the visible (Part IIID) detects a continuum lattice strain associated with an ultrafast generation of the interfacial intermediates. Part IIIA is derived in part from a previous perspective cited by ref.[37] Part IIIB summarizes original work cited by ref.[27, 38] Part III C summarize original work cited by ref.[39] Part IIID summarizes original work cited by ref.[40]

## A. Free energy surface of the photo-excited semiconductor-liquid interface

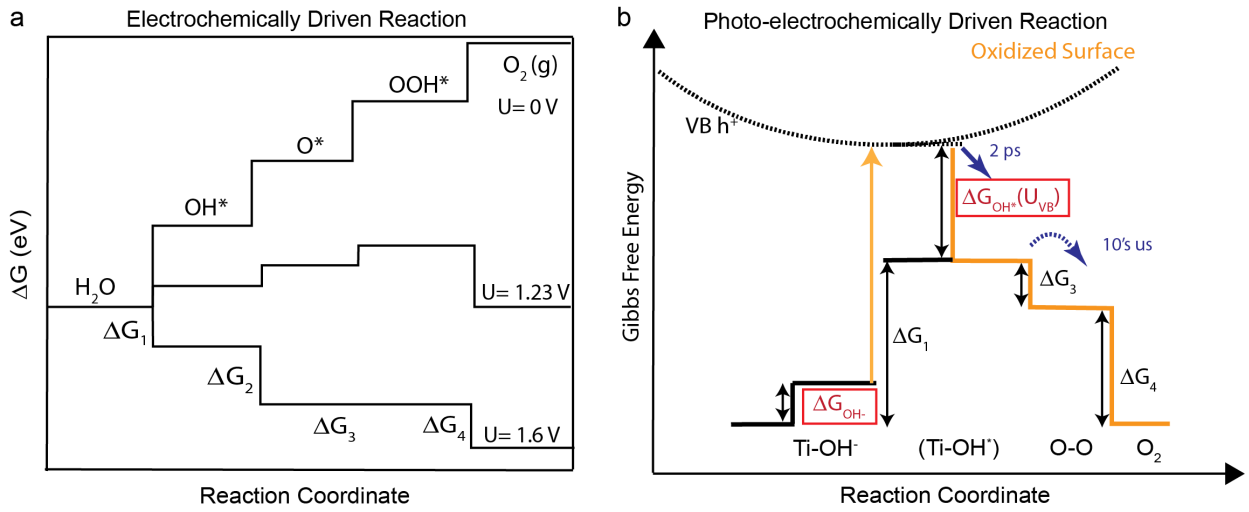


**Figure 10** Free energy diagrams of OER reaction steps depicting a) an electrochemically driven reaction, and b) a photo-electrochemically driven reaction at a semiconducting, transition metal oxide-aqueous interface that has been proposed for n-STO.

The reaction steps cited for the OER mechanism are delineated in Figure 10a, with their reaction free energies: $H_2O/OH^*$ ($\Delta G_1$), $OH^*/O^*$ ($\Delta G_2$), $O^*$/O-O ($\Delta G_3$), and O-O/$O_2$ ($\Delta G_4$). The value of these free energy differences is a function of the electrode potential, from which the electron transfers arise, as shown for a couple of potentials in Figure 10a[24]. Only with enough potential (here 1.6 V vs. the reversible hydrogen electrode, RHE), does each reaction step proceed with a negative $\Delta G$ to evolve $O_2$ spontaneously.

In applying this methodology to the photo-driven reaction at a semiconducting, transition metal oxide-liquid interface, as opposed to a purely potential driven reaction at a metal-liquid interface, one needs to consider two general issues. Firstly, the initial reaction step will be different since the photon excites an equilibrated semiconductor-liquid interface essentially instantaneously.

Secondly, all the reaction steps occur within a fairly large electric field in the aqueous electrolyte that screens the charge in the electrode (the inner & outer Helmholtz layers), which will be different for a metal than the oxide. We address the first point here, since this leads directly to a different manifestation of the first reaction step, which is the focus in the ultrafast regime. A depiction of the photo-driven reaction in terms of free energy differences between intermediate forms is shown in Figure 10b[26]. Prior to light excitation, the sample equilibrates with the electrolyte in the dark (solid black line), for which the relevant reaction is a simple proton transfer modulated by pH and defined by the $pK_a$ of the metal site through the free energy $\Delta G_{OH^-}$:

$$Ti - OH_2 + OH^-(aq) \leftrightarrow Ti - OH^- + H_2O\,(l) \quad Reaction\,(1) \qquad (6)$$

Using the self-ionization of $H_2O$ into $OH^-$ and $H^+$, (1) can be written with a product $H^+$ instead. The representation in equation 5 is convenient if basic pH controls the surface hydroxylation. Such reactions are invoked to explain the interfacial dipole that creates the pH dependent $V_{H,IN}$ (-59 mV/pH) discussed in Part IIB. The scanning methodology described above then helps preserve the starting point of the reaction as that originating from the electrode reaching an equilibrium with the electrolyte in the dark. While this might seem like a small modification, it is important if one would like to define an initial state of the catalyst from which the $O_2$ evolves.

Upon light excitation, VB holes drive the reaction downhill. The free energy diagram therefore has all the subsequent steps of the OER reaction depicted as occurring spontaneously, one after another, such that they can followed causally in time. If holes drive the reaction, the electron-transfer reaction to create the first OER intermediate, M-$OH^*$, is equivalent to the hole-trapping reaction:

$$Ti - OH^- + h^+ \rightarrow Ti - OH^* \quad Reaction\,(2) \qquad (7)$$

$\Delta G_{OH^*}(U_{VB})$ denotes the free energy difference between the delocalized VB hole at $U_{VB}$, the VB edge potential, and the trapped hole. If one adds an electron at the chemical potential of the delocalized hole to each side of reaction (2), the hole-trapping reaction is equivalent to an electron transfer out of the electrode, such that the two reactions net to the first electron and proton transfer from water, or $Ti - OH_2 \rightarrow Ti - OH^* + H^+ + e^-$. The Ti-OH* notation is generic and covers many possible sites of electron transfer in the hydration layer after equilibration with the pH of the electrolyte. In the next sections, we discuss in detail the hole trapping reaction at pH 13 and how it is observed by the transient visible and infrared transitions. Other reviews cover the pH dependencies associated with changing the initial, dark electrolyte condition[7].

## B. Absorption and emission from mid-gap electronic states

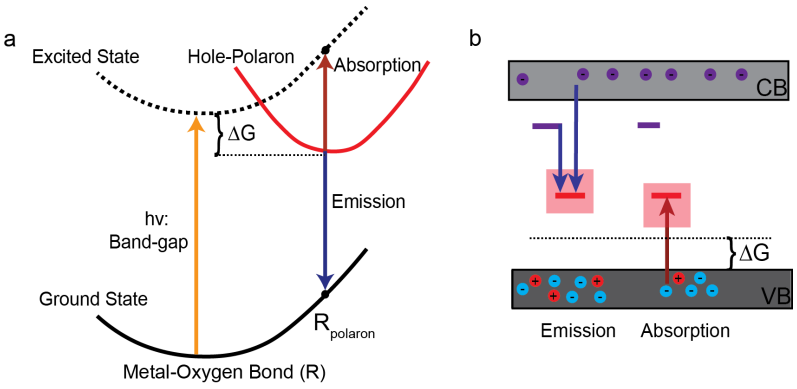


**Figure 11** Absorptive and emissive transitions of hole-polarons in (a) A Marcus diagram showing the vertical transitions involving the hole-polaron potential energy surface (b) A semiconductor band diagram with the red line indicative of the empty, mid-gap hole-polaron density of states. Red, blue arrows/lines denote absorptive and emissive transitions respectively, while ΔG is the free energy difference of hole-trapping. Red band represents the many hole polaron geometries and their associate electronic states.

At the solid-liquid interface, an otherwise delocalized carrier can be trapped by a local polarization that distorts neighboring chemical bonds. The carrier is trapped within a chemical bond distance or more diffusely, across several bond-lengths. The trapped carrier and bond-distortion are together termed a polaron. The connection of the polaron to a reactive intermediate such as Ti-OH$^*$ has only recently been explored[8, 37, 41]. Partly, this is because both a proton and electron transfer are involved in creating Ti-OH$^*$. However, only if $H^+$ and $e^-$ are explicitly in equilibrium after the transfer is the net charge stored in Ti-OH$^*$ compared to Ti-$OH_2$ is zero. Further, as just discussed, for the metal-oxide semiconductor the proton and electron transfer are often treated as sequential steps. Here we first summarize the connections between Ti-OH* and a hole-polaron, that have been explored for a range of 3d metal oxide catalysts in a previous perspective[37]. Then, this sets the stage for how the Ti-OH$^*$ are detected by a broadband visible probe.

| **Table II** | **n-$SrTiO_3$ (Nb 0.1%)** |
|---|---|
| Visible Probe (~eV) | 1.8-3.3 eV (690-375 nm) |
| Refractive index STO ($n_{STO}$) | 2.58 (at 400 nm) |
| Reflected depth: $\lambda/4\pi n_{STO}$ | 12 nm (at 400 nm) |
| Cross-section of $\Delta R/R$ ($\sigma$) | ~10,000 L/mol-cm (at 400 nm) |
| Mid-Infrared Probe (~0.1 eV) | 700-900 $cm^{-1}$ (14-11 μm) |
| Diamond index ($n_1$) | 2.4 |
| Electrolyte index ($n_2$) | 1.12 |
| Evanescent wave depth ($d_p$) | 3 μm (at 800 $cm^{-1}$, 60°) |

At the solid-liquid interface, the local polarization that allows for polaron formation is the interface itself which disconnects the repeated units of the solid from the molecular configurations of the liquid. The surface termination defines the shape of the polaron PES and the "defects" that trap the carrier. As an example, the reactant hole sits in the VB and the Ti-OH$^-$ site represents an electron-dense, hole-trapping site with significant overlap with the bulk VB energy levels. When a hole traps, it becomes the hole-polaron or Ti-OH$^*$. The actual structure of Ti-OH$^*$ depends on the structure of the oxide. Further $H^+$ release to a neighboring site can further trap the polaron within the PES and there are a range of possible configurations, denoted here by (Ti-O$^*$, $H^+$). For photo-excited VB holes that lead to $O_2$ evolution, this reaction is necessarily exoergic with a spontaneous $\Delta G_{OH^*}$.

a

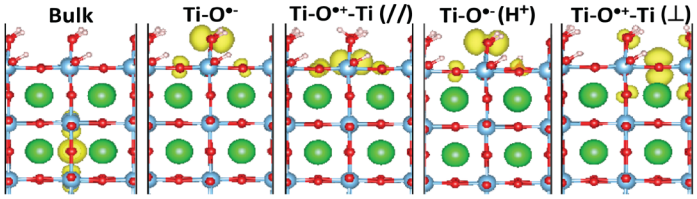


b

| $SrTiO_3$ [a] | Bulk | Ti-O•- | Ti-O•+-Ti (//) | Ti-O•- (H+) | Ti-O•+-Ti (⊥) |
|---|---|---|---|---|---|
| ΔG ($U_{VB}$) (eV) | -0.05 | -0.19 | -0.31 | -0.34 | -0.43 |
| $TiO_2$ [b] | Bulk | OH* | Ti-O•+-Ti | Ti-OH* | Ti-O•- |
| ΔG ($U_{VB}$) (eV) | -0.57 | -0.21 | -0.54 | -0.84 | -1.00 |

**Figure 12** Hole-polaron calculations on STO surfaces that exhibit a range of geometries for Ti-OH* (a) The different hole-polaron/Ti-OH* configurations and the bulk hole-polaron. The two oxyl's differ in the location of the proton. The two lattice oxygen/bridge intermediates differ in the orbital orientation and location of the proton. (b) The free energy difference for hole-trapping to create Ti-OH* on $SrTiO_3$ from ref. a and Ti-OH* on $TiO_2$ from ref. b for the different configurations.

The polarization that stabilizes the polaron can lead to significant changes in M-O bond-lengths and create new electronic states[42]. At a semiconductor surface, these will conveniently occur within the bandgap and for hole-polarons, the quantum mechanical states will be taken from the VB states[37, 43-47]. The creation of the levels within the bandgap allows for optical transitions in the UV, visible, and near-infrared regimes to detect the polarons. Cartoons of the PES for the ground state (black line), the photo-excited state (dotted black line), and the hole-polaron (red-line) are shown in Figure 11a, as a function of metal-oxygen bond length. The metal-oxygen bond length could either increase or decrease depending on the polarization that traps the carrier. The emissive transition is shown as the blue arrow, where conduction band electrons reduce the polaron first at the distorted reaction coordinate ($R_{polaron}$) and then the lattice relaxes back to the minimum of the ground state surface, presumably through phonon modes. For a transition metal oxide surface, this results in recovery of the $Ti\text{-}OH^-$ site that is resonant with the VB levels of the bulk. The absorptive transition is shown as the red arrow, where valence band electrons instead reduce the polaron first at $R_{polaron}$ and then the lattice relaxes back to the minimum of the photo-excited surface, retaining the electron-hole excitation. The $R_{polaron}$ coordinate is the metal-oxygen bond configuration at the minimum in the hole-polaron PES. $\Delta G_{OH*}$ is the free energy difference of the hole-trapping reaction (reaction (2)). As can be seen in this diagram, the $\Delta G_{OH*}$ is not simply related to the vertical optical transitions since distortions are involved. In other words, the metal-oxygen coordinate of the CB and VB is quite different than the one of $R_{polaron}$ such that the electronic component of $\Delta G_{OH*}$ cannot simply be subtracted from the VB edge to identify the mid-gap state.

A simpler band diagram, more often utilized, of these transitions is shown in Fig. 11b. The red line is the mid-gap state formed from the VB. The absorption and emission lines occur from electrons in the VB and the CB, respectively, to this mid-gap state. Therefore, they would add to the band-gap energy, as implied by Figure 11b. However, there are several types of hole-polarons, including bulk and surface polarons of different geometries, to consider and several can occur within the visible regime. Further, in addition to identifying the vertical optical transitions and placing them within the band gap, the transition energy will also depend on: 1) The Franck-Condon overlap for the vibrational structure of the polaron PES 2) Excitonic effects of the electron-hole excitation retained on the photo-excited PES (for the absorptive transition). 3) Effects of dielectric screening of the polaron on the liquid side of the interface.

Figure 12a shows possible configurations of hole-polarons calculated for STO[38] 100 and rutile $TiO_2$[48] 110 and their associated formation free energies (from the VB edge). For the reasons given above, we do not attempt here to associate a particular hole-polaron with the observed optical transitions. In STO, a bulk hole-polaron exists and calculation suggests it gives rise to the 2.5 eV emission from the conduction band, prevalent both in spontaneous and stimulated emission[45]. There are four configurations of Ti-OH* intermediates, two terminal "oxyl" and two lateral "bridge", for which the bridge Ti-OH* (⊥) has largest the formation free energy. In $TiO_2$, a bulk hole-polaron exists and there are again terminal and lateral configurations of various protonation. These calculations were explored to explain the transient absorptive transition near 2 eV in rutile $TiO_2$ 110.[48]

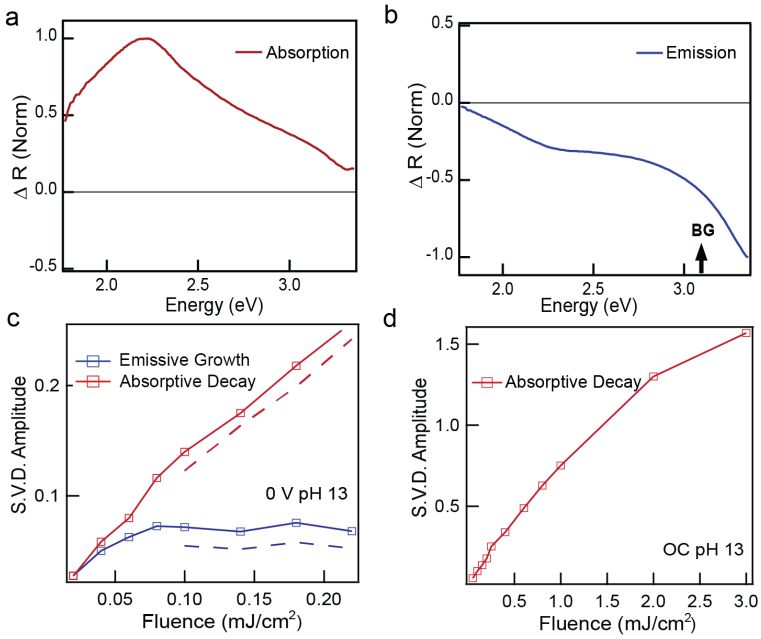


**Figure 13** Absorption and emission of photo-excited STO surface (a) Absorption and (b) Emission spectra obtained from singular value decomposition analysis of broadband spectra at closed circuit and at pH 13. (c) The 1.3 ps emissive growth and the t=0 absorptive decay amplitude from the closed-circuit data at pH 13 as a function of excitation fluence. The amplitude is derived from the singular value decomposition analysis that yields the spectra in a) and b). The solid lines represent 7 um/s scans, while the dashed represent 28 um/s scans. (d) The same for the (t=0) absorptive decay amplitude but taken at open circuit and at pH 13.

Representative transient absorptive and emissive spectra during OER on n-STO are shown in Figure 13a and 13b, respectively[27, 38, 42]. They are derived from an analysis of the raw data shown in Figure 14, obtained by a continuum, broadband probe of 375-770 nm (1.7-3.3 eV). The absorption and emission overlap within the spectral region, requiring that they be separated using a principal component analysis which is detailed elsewhere[7, 27]. In the pump-probe configuration, the emission is predominantly stimulated rather than spontaneous. As might be anticipated, these are broad transitions. The broadness involves not only the Frank-Condon overlap especially considering the distortions involved (Fig. 11a), but also the geometrically diverse (Ti-O*, $H^+$) that are stable and could in principle diffuse.

The data are taken in reflectance, such that one should consider the substrate (n-STO), the surface, and the medium (water) as contributing to the reflectance change. If we treat the surface as a thin film, one in which the Ti-OH* intermediates define its dielectric constant, then one can apply thin film limits to the reflectivity equations. Since 0.1% Nb STO is transparent to below band gap 400 nm light, the appropriate thin film limit is of a transparent substrate. The reflectance change due to the thin film is then derived by McIntyre and Aspnes to be:

$$\Delta R/R \;=\; -4n_1 n_2 \alpha_2 d/(n_1^2 - n_3^2) \quad (8)$$

where $n_3 = n_{STO} = 2.58$, $n_1 = n_{H2O} = 1.33$, d = film thickness, and $n_2$, $\alpha_2$ are respectively the index of refraction and absorption coefficient of the film[49]. The major approximation in reducing the reflectivity changes to the above formula involves $d \ll \lambda$, which should apply to 400 nm probe and an interface that traps charge. A more quantitative way to state this is that in the limit that the film is thinner than the penetration depth of reflected light, $\lambda/4\pi n_{STO}$ (=12 nm), as derived by Riffe and Sabbah, then the absorptive properties of the thin film dominate $\Delta R/R$.[50]

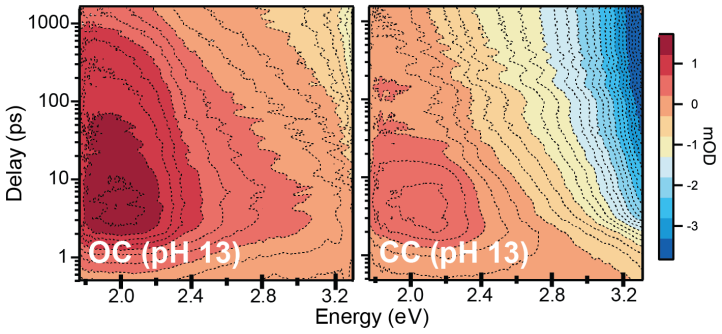


**Figure 14** Transient broadband visible spectra of the photoexcited STO surface Shown are the emissive (blue) and absorptive (red) spectra of the STO surface under open (left) and closed (right) circuit at pH 13 with 400 fs resolution and through 1 ns. These are the broadband and time-resolved data on which the singular value decomposition analysis is performed.

These equations describe real parts with reflected and transmitted probes rather than internal reflectance (the reverse is true for a diamond substrate and the Attenuated Total Reflection geometry in the mid-infrared regime). Thus, the change in reflectivity is proportional to the absorptive properties of the film ($\alpha_2$) if the indices of refraction ($n_1$, $n_2$, $n_3$) are smoothly varying across the probe spectrum. While $n_{STO}$ and $n_{H2O}$ are fairly constant in the visible region (Fig. 3b), $n_2$ should be modulated by the absorptive properties of the film by the Kramers-Kronig relationship. As such, it will appear as a gradual negative and positive change within the width of the absorption whose affect would be to shift the absorptive peak due to $\alpha_2$. With these considerations, the appearance of an absorptive thin film should result in a positive $\Delta R/R$ ($n_1 < n_3$). However, in the pump-probe convention, we utilize $-\log(R_{ON}/R_{OFF})$ to report the optical density (OD) with $R_{ON}$, $R_{OFF}$ given by the reflectance with the pump on, off respectively. Therefore, a positive $\Delta R/R$ will result in a larger $R_{ON}$ than $R_{OFF}$ and a negative OD.

We use these well-developed limits of thin film equations to interpret the sign and magnitude of the observed spectra on STO. Since the absorption change relates to the very surface of the sample and the STO substrate is transparent to 400 nm light, the limit of a thin absorptive film on a transparent substrate should apply. Further, the emissive transition has a negative OD consistent with an additional absorptive layer. The thin film equations are difficult to apply directly to obtain the absorption coefficient $\alpha_2$, since the film thickness d is not known. However, one can employing Beer's law ($\sigma cl$) to obtain the cross-section $\sigma$ instead. If all the holes generated by the laser pulse reaching the surface (such that cl = holes/cm$^2$), the cross-section is on the order of a charge-transfer transition, $\sim 10{,}000 \frac{L}{mol-cm}$.[38] This is consistent with an emissive transition between Ti 3d conduction electrons and unoccupied O 2p orbitals.

The stimulated emissive spectra have a characteristic shape that can be compared with photoluminescence or spontaneous emission measured for STO. The PL contains two prominent peaks at 2.5 eV and 2.8 eV[51-52]. These have been associated with hole-polarons, dopant defects, and defects of the crystal structure (e.g vacancies). As noted above, in particular, the 2.5 eV spontaneous emission has been calculated for near CB band edge electrons reducing a bulk hole-polaron mid-gap state[45]. When measured to high enough energies, the PL has a rising band edge emission near 3.2 eV, seen also in the stimulated emissive spectra (Fig. 13b). In terms of the populations, there could be several origins of this near band edge emission which include: electron-hole recombination, bandgap reduction due to excited state carrier populations, and/or the loss of band states to create mid gap states[37, 47, 53].

The excited state absorption peaks near 2 eV, which has been associated both with a transition of a VB electron to the unoccupied hole-polaron mid-gap state and to intraband transitions within the valence band[54]. A 2 eV transition is in the range anticipated for certain surface hole polarons by theoretical calculations[48]. Understanding how each of these populations—conduction and valence band electrons, valence band holes, and hole-polarons—lead to the optical transitions is both the challenge and a long-term goal of applying ultrafast spectroscopy to the study of OER on a titania surface.

Another way to assess the optical spectra, in the absence of a detailed quantification of its spectrum, is to tune relevant reaction conditions to modulate the emissive and absorptive spectral signatures. As can be seen in the raw transient optical data of Figure 14, there is a difference between the closed and open circuit spectra with an increase of the emissive component in closed circuit. In OC, since the electrons are not allowed to complete the circuit, they will recombine with the holes. In CC, the circuit with the counter electrode is complete and the resulting photocurrent was detailed in Part IIB. The difference suggests that the emissive spectrum measures the hole-polaron population associated with OER. Further assessments are made through the observed kinetics and correlations with exciting higher electron and hole populations. Figure 13c and 13d shows the behavior of the absorptive and emissive components with excitation fluence. For the absorptive component, the amplitude is of the ultrafast rise, within the time-resolution of the pump-probe cross-section (400 fs) that then decays. For the emissive component, the amplitude is of the time constant with a 1.2 ± 0.3 ps growth. While not shown here, these time constants can be derived from fitting select wavelengths or performing the principal component analysis. The absorptive spectrum grows linearly with fluence for both closed and open circuit conditions, up to 3 mJ/cm$^2$. On the other hand, the emissive spectrum already saturates by 0.1 mJ/cm$^2$, which is approximately ~ 4% of the available surface O-sites. The absorptive component dominates at open circuit and so the saturation is shown only for the closed-circuit conditions.

There is a clear dichotomy between the absorptive and emissive signals: the emissive signal dominates at CC, exhibits a rise time, is metastable, and saturates with laser fluence, while the absorptive signal dominates at OC, occurs within the resolution of the experiment, decays, and linearly increases with laser fluence. The characteristics of the emissive transitions are also consistent with a new, absorptive layer as analyzed by the thin film equations. The challenge now

is to see whether one can correlate the energies of the optical transitions to the population dynamics observed, which will require a closer collaboration with theory.

## C. Infrared attenuated total reflectance of vibrational normal mode of Ti-O$^{*-}$

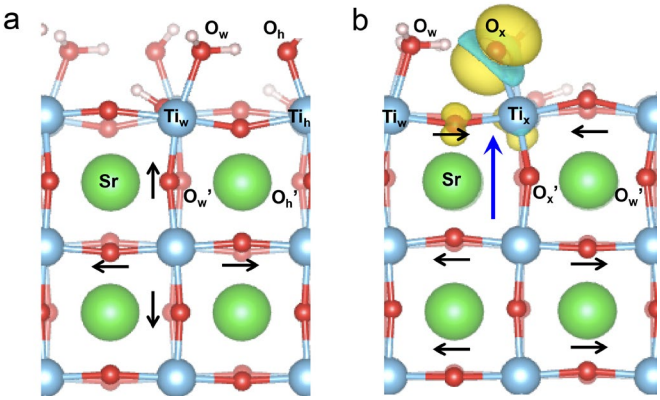


**Figure 15** Infrared activity of oxyl radical (a)The water adsorbed $SrTiO_3$ surface before illumination. The mode shown is a bulk breathing motion present in the dark and IR-inactive. (b) The water adsorbed $SrTiO_3$ after illumination. Changes in electron spin density (decrease – yellow, increase – cyan) indicative of hole capture to $O_X$ results in a surface Ti-O$^{\bullet-}$ termination. The presence of Ti-O$^{\bullet-}$ generates a new, surface, IR active mode because of a large amplitude motion of $O_X$' that disrupts the original breathing mode.

One of the successes of the transient spectroscopy of OER on STO was the identification of a normal mode for a particular configuration of (Ti-O$^*$, H$^+$) the titanium-oxyl, where the hole traps on the terminal oxygen (Ti-O$^{\bullet-}$) (Figure 15)[39]. The normal mode is a motion of the sub-surface oxygen underneath the titanium oxyl. In the following, the critical factors necessary to experimentally detect this mode and make the assignment are described. The reflectance used to detect the mode is attenuated total internal reflectance (ATR) that generates an evanescent or decaying mid-infrared wave. The ground state phonon structure of STO as seen by a usual propagating reflective probe is first described and then contrasted with an evanescent wave probe

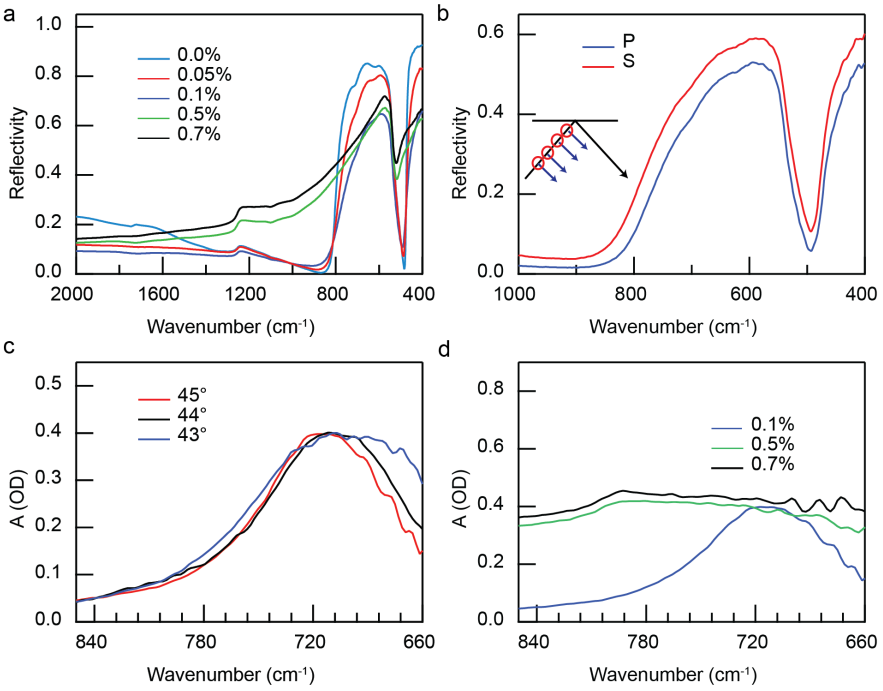


**Figure 16** Infrared reflectance of the n-$SrTiO_3$ surface. (a) Reflectance as a function of electron doping (Nb), (b) S & P polarized reflectance of 0.1% Nb STO, showing no polarization dependence for a simple reflectance measurement. (c) Attenuated total reflectance of 0.1% Nb STO as a function of incidence angle with P-polarized light, and (b) Attenuated total reflectance as a function of doping (Nb) with P-polarized light. Cartoon in b) shows the S- and P- polarized light vectors in the ~ 45° geometry; dots represent vectors perpendicular to the plane of incidence.

of the STO/electrolyte interface. Next, the excited state ATR cross-section is elucidated. This description includes how an evanescent wave is incorporated in a full, 3-electrode photo-electrochemical cell that can modulate reaction conditions. Next, the mid-infrared mode seen experimentally by ATR of the excited state surface of STO is shown. Here, the focus is on when the mode occurs as a function of changing the reaction conditions, such as open and closed circuit and excitation fluence. Other reviews cover the shape of the mode, which is a Fano resonance[55] with the surrounding continua of the solid (plasma excitations of the dopants) and the liquid (water librations). Finally, the theoretical calculation which aids in unambiguously assigning the mode is described.

*Infrared reflectance:* Static infrared spectra of the samples were measured by specular reflectance (45° incidence) using a Fourier transform IR spectrometer; a protected gold mirror was used as reference. External reflection spectra (un-polarized) of doped and undoped $SrTiO_3$ are shown in Figure 16a. The results are consistent with those previously reported in the literature for both undoped and doped STO. Two poles in the imaginary part of the dielectric constant, one at 530 $cm^{-1}$ and one at 795 $cm^{-1}$, can be extracted using a Kramers-Kronig transform of the undoped and 0.1 % Nb doped samples[32]. The 535 $cm^{-1}$ peak is assigned to a transverse optical (TO) phonon and the 795 $cm^{-1}$ peak is assigned to a longitudinal optical (LO) phonon. For higher doped samples (0.5% and 0.7%), the reflection spectra differ from that of the undoped and 0.1% Nb doped samples due to the coupling of the LO phonon to the plasma density.

Spectra of 0.1% Nb STO with S and P polarized light are shown in Figure 16b. S-polarized light has an electric field that is in the sample plane, while P-polarized light has a component that is out of the sample plane depending on the angle of incidence. At 45°, 50% of the intensity will probe the transition dipole out-of-plane. For a single crystal sample, bulk LO phonons that propagate in the same direction as their electric field cannot be excited by light unless they couple to TO phonons or a transverse electron plasma (REF). This is exemplified by the lack of a polarization dependence in reflectivity at 795 $cm^{-1}$ where an LO phonon, with a dipole perpendicular to the sample plane, is expected. In contrast, a molecular vibration will exhibit polarization dependence indicative of the direction of its dipole.

*Attenuated total internal reflection spectra:* Attenuated total internal reflection (ATR) spectroscopy uses internal reflection within an ATR crystal to create an evanescent infrared wave that probes the single crystal surface. The evanescent wave cannot couple directly to a propagating, optical phonon in the bulk because the wave decays spatially with distance from the ATR crystal, while the TO and LO are propagating modes that exist throughout the solid. This is evident in the static ATR spectra of the STO samples in air, which are shown in Figure 16c and Figure 16d. For these measurements, the internal reflection in air (i.e. without a sample present) was used as a reference. In the 0.1% Nb STO sample, a broad mode occurs centered at 710 $cm^{-1}$, while in the 0.5% or 0.7% Nb STO samples, no clear mode is present. The mode seen in 0.1% Nb STO has been previously assigned to a surface LO polariton by its appearance in P-polarized light alone and its shift with incident angle (Figure 16c)[56]. A surface LO polariton is a P-polarized light wave that couples to a surface optical phonon propagating along the sample plane. The surface

polariton becomes much broader for the higher doped samples, which is likely a result of coupling to the electron plasma density.

In this geometry, a single STO crystal needs to be placed within the evanescent wave generated at the ATR crystal interface. There are other geometries for ATR measurements, which include a thin film on the ATR crystal. However, in the thin film geometry, if the evanescent wave hasn't fully decayed, it will allow for reflections that could then allow direct coupling to the bulk phonon modes, as has been observed an STO thin film[57]. The ATR crystal used for the experiments is a single bounce diamond cell (Figure 17a). The single bounce allows for a facile pump-probe overlap between the UV pump beam and the mid-IR probe. The diamond is transparent to both the mid-IR beam in the region of Ti-O stretches and the UV pump beam. To position the STO single crystal within the evanescent wave, a piezo-electric stepper motor is utilized to step the z-distance ($\Delta Z$). The following equation gives the $\frac{1}{e}$ decay distance of the evanescent wave's electric field[58]:

$$d_p = \frac{\lambda}{2\pi\sqrt{{n_1}^2 sin^2(\theta) - {n_2}^2}} \qquad (9)$$

A value of $d_p \approx 1.1$ μm is obtained for the 60° angle of incidence in the transient experiments, at 800 $cm^{-1}$, and for the diamond ($n_1$=2.4)/electrolyte ($n_2$=1.12) interface. When a 0.7% Nb doped STO sample is stepped towards the diamond by the piezoelectric motor, the light throughput attenuates from its maximum value as the STO single-crystal enters the region of $d_p$ (Figure 17b) The light attenuation is attributed to free carriers excited by the mid-IR light in STO. The dotted line indicates when the sample is considered pressed to the diamond surface. To repeatedly position the sample between experiments, the sample position is scanned and then returned to the position with half the magnitude when pressed.

In addition to the mid-IR light attenuation, the transient signal observed near 800 $cm^{-1}$ in the pump-probe experiments increases as the STO single-crystal enters the region of $d_p$. This can be understood from the equation that governs the absorption change of the transient signal[39, 58]:

$$\Delta R/R = -log\left(\frac{I_0 - I_0\left(\frac{n^{ON}\kappa^{ON}|{t_{12}}^2|}{n_1 cos(\theta)\sqrt{{n_1}^2 sin^2(\theta) - {n_2}^2}}\right)e^{\frac{-2\Delta Z}{d_p}}}{I_0 - I_0\left(\frac{n^{OFF}\kappa^{OFF}|{t_{12}}^2|}{n_1 cos(\theta)\sqrt{{n_1}^2 sin^2(\theta) - {n_2}^2}}\right)e^{\frac{-2\Delta Z}{d_p}}}\right)$$
$$= -log\left(\frac{1 - T^{ON}}{1 - T^{OFF}}\right) \qquad (10)$$

In the above, $n^{ON}$, $\kappa^{ON}$, $n^{OFF}$, $\kappa^{OFF}$ represent the real and imaginary indices of refraction with pump light on and pump light off. If the sample is a weak absorber and there is no change in the refractive index n upon excitation, $\Delta R/R$ simplifies to a change in absorption:

$$\frac{\Delta R}{R} = \Delta A = (\kappa^{ON} - \kappa^{OFF}) e^{\frac{-2\Delta Z}{d_p}} \qquad (11)$$

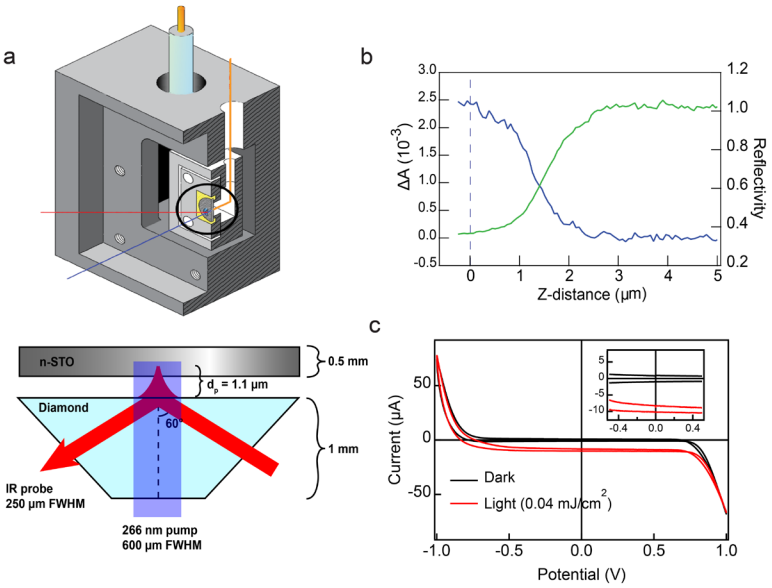


**Figure 17** Attenuated total reflection photo-electrochemical cell a) Cross-section of cell with the reference, working, and counter (not-shown) electrodes and the pump (blue) and probe (red beams). Bottom is a close-up of the diamond ATR crystal and STO. b) The absorption change (blue, left) and ground state reflectivity (green, right) of the probe as a function of distance (ΔZ) from the ATR crystal. c) Dark and light cyclic voltammagram of STO within the cell. Inset shows 10 uA photocurrent, equivalent to 56% quantum efficiency.

The simplified relation serves to highlight an ATR-specific property. As the sample is positioned closer (smaller $\Delta Z$) to the diamond, there is greater overlap between the sample and the evanescent electric field, such that the differential pump-probe signal increases.

However, the sample is not a weak absorber since the free carriers alone can reduce the probe throughput substantially. Further, continua on both sides of the interface in the same frequency range exist that could readily change upon excitation. The two continua are the free carrier and plasmonic excitations of the n-dopants on the solid side[59] and librational motion of water on the liquid side[60]. Through the Kramers-Kroning relation that derives n from κ, changing the absorption cross section via $\kappa^{ON}$ also modifies $n^{ON}$ in the same spectral region. Further, by the continua, photoexcitation will change n, κ over a larger spectral range than is being measured. Therefore, to truly determine the absolute change in the absorptive cross-section ($\kappa^{ON}$ - $\kappa^{OFF}$), the Kramers-Kronig relation for n and κ over a large frequency range should be consistently incorporated into the ATR equation. Only if this is done consistently could one interpret both the sign and magnitude of ΔR/R in terms of the real and imaginary refractive indices. For example, the 0.7% Nb STO ATR cross-section is negative, while for 0.1% Nb STO, it is positive. Understanding this change based on the continua involved and the refractive index changes is not attempted as it requires taking data out to far infrared frequencies. On the other hand, the shape of the spectrum in the narrow spectral range of the mode will be determined predominantly by the absorptive part, or $\kappa^{ON}$ - $\kappa^{OFF}$.

*A full 3-electrode photo-electrochemical cell:* The ATR probe of the STO/electrolyte interface needs to be situated within a full 3-electrode, photo-electrochemical cell. At a minimum, this requires the placement of three electrodes and their leads, the working electrode (STO), the counter electrode (Pt), and the reference electrode (Ag/AgCl). They should not contact eachother and should be robust against breakage. Since the counter and reference are simply placed at a distance from each other and the working electrode, they are independently accommodated. Special care

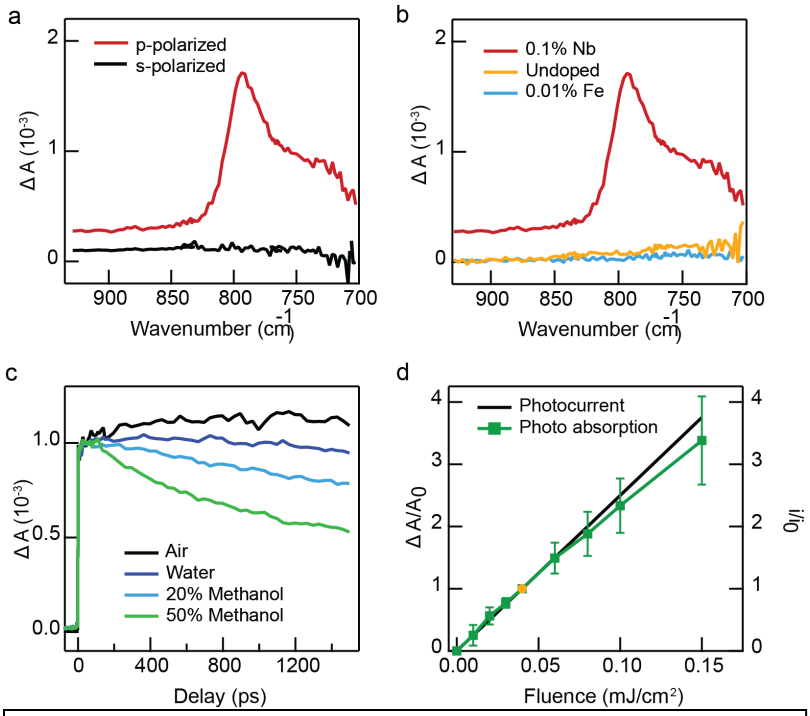


**Figure 18** Transient oxyl mode of n-$SrTiO_3$ by ATR as a function of: a) the incoming light polarization (S and P), b) doping (n-, p-, and undoped), c) time-delay in different electrolytes where methanol is a scavenger, and d) its correlation with $O_2$ evolution. Error bars in ΔA represent the standard error over three trials. ΔA and *i* have been normalized to their respective value (solid yellow dot) at a fluence of 0.04 mJ $cm^{-2}$.

must be taken for the working electrode and lead, and most of the cell-design concerns its placement. If not designed to prevent it, breakage of the working lead is common since it needs to be bent to reach the top of the cell and further, the working electrode is moved by the piezo-electric motor. The most recent design for the photo-electrochemical cell is the one shown in Figure 17a, where the working electrode lead is accommodated in a separate area to decouple its motion from the surrounding cell; this also has the advantage that the working lead doesn't touch the electrolyte if the o-ring is well-sealed. Besides the front plate that accommodates the diamond ATR crystal, the cell is made of a hard Teflon. The placement of the working and reference leads are shown on the electrochemical cell cross-section. The ATR crystal, the sample, and how the infrared beam couples in is also shown. A closer view of this cross-section highlights the dimensions of the evanescent wave. An example of cyclic voltammetry curve using the ATR photo-electrochemical cell in the dark and under light excitation is shown in Figure 17c.

*The transient infrared spectrum probed by an evanescent wave:* This experimental setup allowed the surface vibrational mode of the oxyl to be observed upon photoexcitation of STO (Figure 15). The spectrum of the photo-generated mode (Figure 18)[39] peaks at 795 $cm^{-1}$ (± 3 $cm^{-1}$), which is near the bulk LO mode frequency. The narrow bandwidth of the signal (35 $cm^{-1}$, 4 meV) and its appearance in the frequency range known for Ti-O stretches identify a vibrational rather than an electronic transition. Moreover, the same narrow mode occurs over a wide range of doping (Nb 0.1% to 0.7%) that would necessarily modify the width of an electronic transition. The mode (Fig. 18a) solely occurs in P-polarization of the infrared probe beam. Given that in the ground state only the surface polariton is observed and that bulk LO optical phonons do not exhibit a polarization dependence, the exclusive appearance of the mode in P-polarization identifies it as a molecular, surface localized vibration with a dipole perpendicular to the sample plane. Therefore, the mode is characteristic of a new transient species rather than a change in the dipole or occupation of a ground state mode. As noted above, the sign of the transient species, when measured by ATR

of the solid-liquid interface, cannot be interpreted via Beer's law and a new absorptive cross-section can appear as either a positive or negative differential signal.

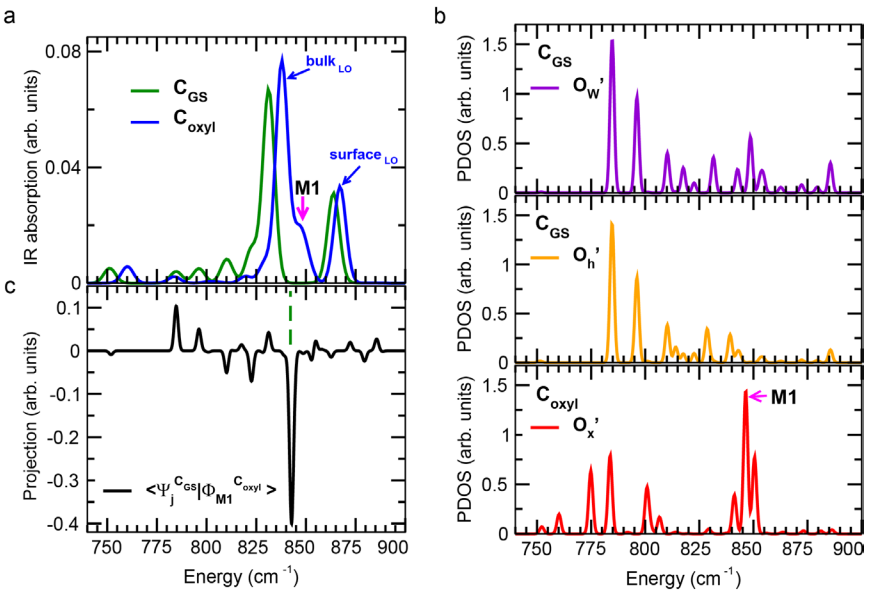


**Figure 19** Theory of surface-related modes. Infrared activity of the ground state configuration ($C_{GS}$) and the oxyl configuration ($C_{oxyl}$) and associated phonon density of states for different surface related O sites ($O_h$', $O_w$' $O_x$') within the two configurations. a) Infrared activity of the slab for $C_{GS}$ and $C_{oxyl}$ where M1 indicates the new surface mode upon creating the oxyl. b) Partial density of states of $O_w$' sites in $C_{GS}$ (top), $O_h$' in $C_{GS}$ (middle) and $O_x$' in $C_{oxyl}$ (bottom). c) Projection of the eigenvector of mode M1 in $C_{oxyl}$ on the phonon eigenvectors of $C_{GS}$, where the primary contribution comes from a dark breathing mode at 843 cm$^{-1}$.

The mode is attributed to a hole-trapped species by: (1) its appearance only with photo-excited charge separation at the n-STO interface (Fig. 18b), (2) a long lifetime that decreases as a function of methanol concentration (Fig. 18c), and (3) its correlation with $O_2$ evolution (Fig. 18d). The mode occurs exclusively in n-doped samples, while it is completely absent in un-doped and p-doped samples that have low quantum efficiency for charge separation and $O_2$ evolution (< 1%). The lifetime of the signal at 795 cm$^{-1}$ demonstrates a very long-lived vibration (> 1 ns). This long lifetime excludes an assignment to a highly excited Ti-O surface mode of the ground state. Further, the lifetime decreases substantially as a function of methanol concentration in water, such that the photo-hole generated transient species occurs uniquely at the water-adsorbed surface and is quenched by a better hole acceptor. Finally, the full 3-electrode electrochemical cell that accommodates the ATR probe beam allowed for the correlation of the hole-trapped population with $O_2$ evolution. Namely, as the current for $O_2$ evolution increases with excitation fluence, the measured population increases. The measurements are done in a limited range of fluence (< 0.2 mJ/cm$^2$ ) since the surface excitation of holes saturates, as discussed above for the stimulated emission in the visible.

*Theoretical mode assignment of sub-surface vibration to Ti-O*$^{*-}$: While the data demonstrate that a transition dipole for a surface-localized, Ti-O vibration becomes bright whenever a hole sits at the surface, assigning that vibration to a particular species and its vibration required theoretical calculations[39]. A water-adsorbed and undoped $SrTiO_3$/air interface with holes was the starting point for a more detailed, molecular description of the vibration and the associated transient species using first-principles theory. At equilibrium, a partially dissociated configuration ($C_{GS}$), wherein 50% of adsorbed water molecules lose an H atom to one of the lattice surface oxygen atoms and

hydroxyl-water dimers form (Fig. 15a). This was also confirmed for undoped STO, and recently for lightly (0.1% Nb) surfaces by AP-XPS as discussed in the surface characterization section of part II. In the photo-excited configuration ($C_{oxyl}$), the hole is localized on a terminal O adatom ($O_x$) and there are two hydroxyl groups on the surface $TiO_2$ layer (Fig. 15b). While holes can localize both on lateral and terminal O-sites, localizing the hole at a lateral oxygen surface site does not lead to out-of-plane polarized vibrations, as observed in experiment.

Phonon frequencies and eigenvectors for configurations $C_{GS}$, $C_{oxyl}$, and a pristine surface are calculated using a density functional finite difference approach, and associated infrared absorption oscillator strengths are obtained using an established methodology[61]. The dominant motion for the Ti-O modes observed in P-polarization (perpendicular to the surface) is related to either the O in SrO layers or the adsorbed atoms ($O_w$, $O_h$, $O_x$) defined in Fig 15. The vibrations of O sites within the SrO layers can be divided into bulk O modes ($O_{bulk\text{-}SrO}$), sub-surface O modes of the un-terminated layer ($O_{bottom\text{-}SrO}$), and the sub-surface O modes of the terminated layer ($O_w'$, $O_h'$ and $O_x'$). In both $C_{GS}$ and $C_{oxyl}$, the bulk LO Ti-O mode occurs near 835 $cm^{-1}$ (bulk LO in Fig. 19a). A surface infrared active LO Ti-O mode of $O_{bottom\text{-}SrO}$ occurs at 866 $cm^{-1}$ (surface LO in Figure 19a).

The significant difference in infrared activity between $C_{GS}$ and $C_{oxyl}$ appears at 846 $cm^{-1}$ (Fig. 19a) where $O_x'$ is decoupled from the $O_w'$, $O_h'$ motion and dominates the projected phonon density of states (PDOS) (Fig. 19b). As can be seen from projecting the new eigenstate (M1 in Fig. 19a) in $C_{oxyl}$ on the $C_{GS}$ eigenstates, the dominant contributor to M1 is an originally dark (infrared-inactive) mode in $C_{GS}$ at the same energy and the remaining spectral weight is distributed among many (infrared active and dark) modes in $C_{GS}$ (Fig. 19c). The dark breathing motion in $C_{GS}$ (Fig. 15a) is disrupted by a large new amplitude motion on $O_x'$ (Fig. 15b). We can assign M1 to the Ti-O infrared activity seen experimentally because: (1) it occurs at a frequency ≈ 10 $cm^{-1}$ above the bulk LO Ti-O mode; (2) it is associated with an oxyl radical, or a photo-hole active site; (3) it is associated with a completely new absorption cross-section not seen in the ground state; (4) it does not involve a proton such that the frequencies do not change upon deuteration (as shown in the original publication[39]); (5) the infrared activity comes from a sub-surface layer whose transition dipole is out-of-plane polarized; and (6) can readily couple to bulk and surface water librations (as shown in the original publication[39]).

Furthermore, as shown in Fig. 19a, M1 is the distinctive infrared mode associated with the oxyl radical. One might also expect to observe a beating mode of the surface oxyl Ti-$O_x$ bond itself, but only weak and spectrally broad IR activity is predicted for motions of Ti-$O_x$ at the fully water-adsorbed surface; hydrogen bonding strongly hybridizes the motion of $O_x$ with nearby surface-adsorbed water groups. Thus, a pure Ti-$O_x$ beating mode is not expected to be a stable vibrational eigenstate of the oxyl radical.

### D. Coherent acoustic interferometry of lattice strain

The hole-trapping reaction that leads to (Ti-$O^*$, $H^+$) introduces lattice distortions of the metal-oxide reaction coordinate, or hole-polarons. As measured by transitions to new electronic states in the visible regime and new normal mode vibrations in the mid-infrared regime, these lattice

distortions are local over a site or several connected sites. If a population is created, these local distortions could also introduce non-local distortions of the continuum lattice. In other words, they could change the size of the repeated periodic unit cell through a strain generated at the interface. In this section, the coherent acoustic interferometry technique that detects such a strain due to hole trapping at the STO/electrolyte interface is reviewed[40]. The importance of associating the interfacial strain with the hole-polaron population is two-fold: 1) it directly sees a distortion of the metal-oxygen coordinate, even if a non-local one, and 2) it completes the detection of ($Ti\text{-}O^{*}$, $H^{+}$) across the electromagnetic spectrum by extending the visible and mid-infrared detection of electronic states and vibrational normal modes to the GHz regime of long-wavelength phonons.

*Coherent Acoustic Interferometry of STO/electrolyte & the Dispersion Relationship.* As summarized in Fig. 20, the optical technique works by first generating a laser-triggered interfacial strain) which results in a propagating acoustic strain pulse into the bulk. The optical probe pulse scatters off this propagating strain pulse and interferes with surface reflected probe beams to generate coherent acoustic waves (CAWs) in the data, defined by their oscillation frequency, amplitude, and phase response as a function of optical wavelength (Fig. 20a and 20b). This technique is usually associated with detecting strain arising from delocalized electron-hole pair creation and/or separation[62]. The delocalized electron-hole pairs can distort the lattice by thermalizing to the band edges and releasing heat or directly coupling to phonons through a deformation potential[62]. We summarize here how coherent acoustic interferometry was newly applied to ultrafast excitation of OER at the n-STO/electrolyte interface. As described below, both strains associated with delocalized carriers and with the trapped holes are detected with very different phenomenology.

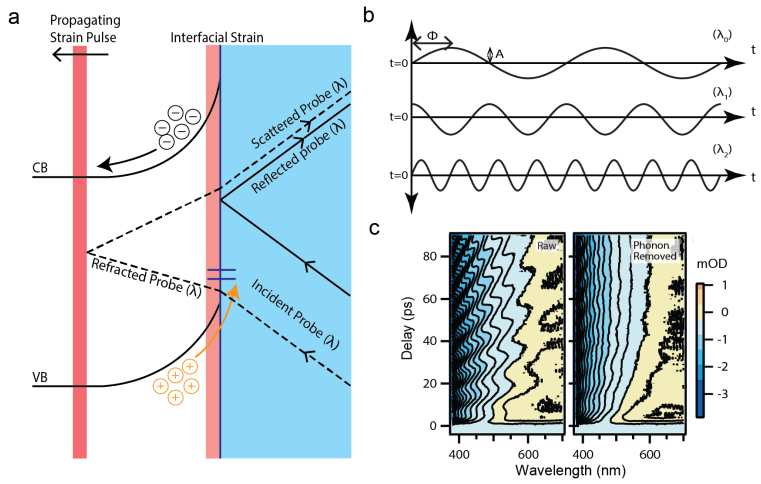


**Figure 20** Overview of polaron-induced strain and detection of its propagating acoustic strain pulse. a) Band gap excitation generates carriers, which separate due to the depletion layer. Holes trap at the surface (panel C) and cause an interfacial strain. Ultrafast generation of the strain launches a propagating strain pulse into the bulk, detected as an interference pattern between the surface reflected probe and acoustically scattered probe. These are the coherent acoustic waves (CAWs). b) As the pulse propagates into the bulk and the pathlength difference between the reflected and scattered probe increases, the CAWs oscillate in time with frequencies that change as a function of probe wavelength. These oscillations are also characterized by their amplitude and phase. c) The CAW oscillations seen in the data (raw) for 0.1% Nb STO at pH 13 in closed circuit. They can be removed by modelling their frequency, phase, and amplitude (phonon removed).

Figure 20c shows the coherent acoustic waves seen in the data. The data were taken for both OC and CC conditions with bandgap excitation. Both OC and CC spectra contained prominent ~50-100 GHz oscillations. They are an additive contribution to the absorptive and emissive optical transitions. The below summarizes how the frequency, amplitude, and phase of these oscillations are extracted from the data. These are then used to link the CAW in the CC

condition to interfacial strain generated by a hole-polaron population. The OC condition is used as a foil, in which the CAWs derive instead from high populations of photogenerated delocalized carriers.

The wavelength-dependent oscillation frequency, amplitude, and phase is extracted by fitting the TR kinetic traces for each wavelength to a sum of two growth exponentials, a decay exponential, and oscillatory components that models CAWs in STO and water:

$$\Delta OD = G_{fast} + G_{slow} + D_1 + CAW_{STO} + CAW_{H2O}, \quad (12a)$$

$$G_i = -A_{G,i}\left(1 - \exp\left(-t/\tau_{G,i}\right)\right) \quad (12b)$$

$$D_i = A_{D,i}\exp\left(-t/\tau_{D,i}\right) \quad (12c)$$

$$CAW_i = A_{CAW,i}\exp\left(-t/\tau_{CAW,i}\right)\cos(\Omega_i t + \phi_i) \quad (12d)$$

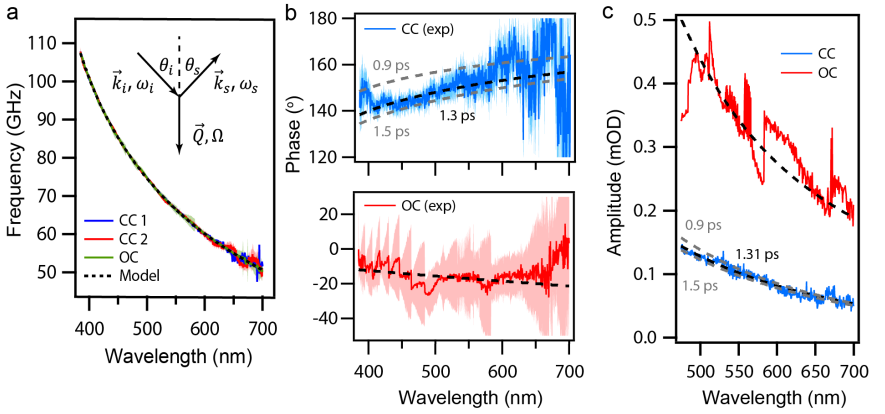


**Figure 21** The frequency, phase, and amplitude of the CAW. a) CAW frequency, $\Omega(\lambda)_{STO}/2\pi$, as a function of probe wavelength as extracted by the fit for one OC data sets and two CC data sets. The inset shows the wavevectors for the SBS phase matching conditions and the dotted line is a fit to its dispersion. b) The CAW phase, $\phi_{STO}$, as a function of wavelength for one OC and two CC data sets as extracted by the fit. c) The CAW amplitude, $A_{CAW,STO}$, as a function of wavelength for OC and two CC data sets as extracted by the fit. The dotted lines in b) and c) are the result of the model when an interfacial strain is input, as described in the text. For all panels, OC conditions were acquired at pH 13 with a pump fluence of 2.0 mJ/cm$^2$ and CC conditions were acquired at pH 13 with a pump fluence of 0.04 mJ/cm$^2$. The shaded regions of b, represent the standard error bounds from the least squares fit.

The two growth exponentials in eq. 12a represent the growth of an emissive signal associated with hole trapping and the decay exponential is associated with the decay of the delocalized carriers[38]. For hole trapping, we found that the average fast growth timescale was 1.2 ± 0.3 ps[40]. The two CAW terms are associated with acoustic pulse propagation in STO and in the aqueous electrolyte. The CAW signal from the water is a ~5-10 GHz signal not the focus of the discussion here.

The wavelength dependent fit results for the n-STO CAW oscillation frequency, phase, and amplitude are shown in Figure 21a, 21b, and 21c respectively. We will return to the oscillation phase and amplitude below. The oscillation frequency as a function of probe wavelength matches the stimulated Brillouin scattering (SBS) phase matching condition almost exactly (Fig. 21a). The SBS phase matching condition is given by,[63-64]

$$\frac{\Omega}{2\pi} = \frac{2vn}{\lambda}\cos\theta_i, \quad (13)$$

where $\lambda$ is the probe vacuum wavelength, $n(\lambda)$ is the real part of the index of refraction in 0.1% Nb:STO, $v$ is the acoustic velocity in STO,[65] and $\theta_i(\lambda)$ is the incidence angle of the probe in STO. In addition, the CAW in water also closely follows this relation, with the corresponding refractive index, acoustic velocity, and incidence angle. For STO, the physical picture that follows is cartooned in Fig. 20a: the interference of the surface reflected probe and transmitted probe scattering from an acoustic, bulk propagating strain pulse.[63, 66] This acoustic strain pulse is a direct result of ultrafast strain generation just below the STO surface, which describes uniaxial expansion (tensile strain) or contraction (compressive strain) of the STO lattice in a direction normal to the surface.

*Correlating Coherent Acoustic Wave Amplitude with Emission and Absorption.* To gain more insight into the source of the interfacial strain, the CAW amplitude is correlated against the amplitudes of the fast emissive component and absorptive component with pump fluence for OC and CC conditions. The emissive and absorptive components are the same as that described in PartIII B extracted by a principal component analysis. Their fluence dependence is shown in Figure 22. To compare the CAW amplitude to these emissive and absorptive components, the kinetic traces were fit to the exponential parts ($G_{fast}$, $G_{slow}$, and $D_1$) of eq. 10a to extract a condition-dependent absorptive amplitude which arises within the excitation pulse width (<400 fs) and a condition-dependent emissive amplitude which is formed with a ~2 ps time constant.

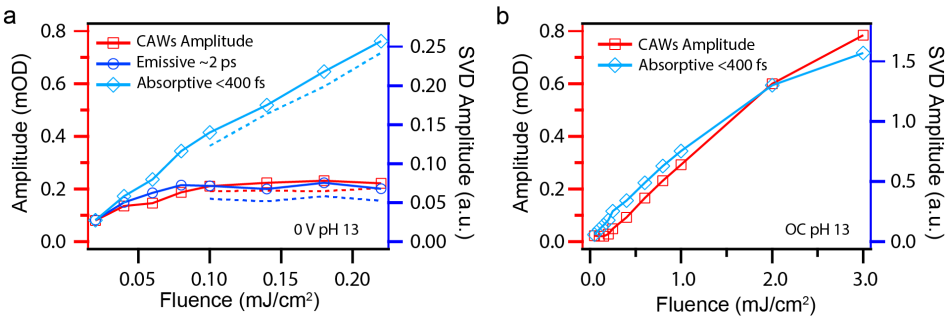


**Figure 22** Correlating CAW amplitude to absorption and emission. a) Fluence dependance of CAW amplitude for CC in pH 13. Here, the CAW amplitude (red squares, left axis) correlates with the ~2 ps emissive amplitude (dark blue circles, right axis), but not with the <400 fs absorptive amplitude (light blue diamonds, right axis). To show that the effects of surface degradation do not influence the correlation, the solid lines were acquired with a scan speed of 7 µm/s while the dashed lines were acquired at 28 µm/s. b) Fluence dependance for OC in pH 13 showing that the OC CAW amplitude (red squares, left axis) correlates with the <400 fs absorptive amplitude (light blue diamonds, right axis). For all panels, the ~2 ps emissive amplitude and <400 fs absorptive amplitude were extracted by fitting kinetic components from the SVD analysis.

As described above, the visible reflectance spectra at OC are dominated by a decaying absorptive component that forms within the pump pulse duration, which we therefore associate with the delocalized carrier population. In contrast, under CC conditions, the spectra are dominated by a ~2 ps emissive rise that becomes meta-stable such that it is associated with the trapped hole-polaron population. When varying pump fluence, the correlation between the CAW amplitude and the emissive amplitude is present only under CC conditions and not under OC conditions. As shown in Fig. 22a, the CC CAW amplitude (red squares) and emissive amplitude (dark blue circles) both exhibit a saturation behavior as the pump fluence is increased, while the absorptive

amplitude (light blue diamonds) grows linearly with fluence. In contrast, the OC CAW amplitude (Fig. 22b, red squares) closely follows the nearly linear increase of the absorptive amplitude (light blue diamonds) and does not exhibit any saturation behavior for the wide range of fluences measured. Further, when normalized for fluence, the CAW signal is approximately 10 times stronger in CC as compared to OC within the CC linear regime. That the CAW amplitude correlates with the saturation behavior of the ~2 ps emissive amplitude attributes the CC generation to hole-polaron formation. On the other hand, the linear correlation of the CAW amplitude with fluence that patterns the absorptive amplitude, along with its less efficient excitation, attributes the strain formation in OC to a high photo-carrier population.

*Coherent Acoustic Wave Phase.* The CAW phase (Fig. 22b) and amplitude (Fig. 22c) spectra were modeled in terms of the sign, magnitude, spatial extent, and formation time of the interfacial strain that generates the propagating strain pulse. This model extends the one initially developed by Thomsen, et al.[63] in the acoustic interferometry regime[67] by including a strain formation time and broadband response. The CAW phase spectrum is the primary focus. A similar formation time vs. phase analysis has also been performed by Babilotte, et al.[68] The strain wave propagating into the bulk (z-direction) is modelled as:

$$\varepsilon_{zz}^{T}(z,t) = \varepsilon_0^T S\left(\frac{z}{\xi}\right)\left(G\left(\frac{t}{t_0}\right) * \frac{P\left(\frac{t}{\sigma}\right)}{\sigma}\right), \quad (12) \text{ where:}$$

$$S(x) = \theta(x)e^{-x},$$

$$G(x) = \int_{-\infty}^{x} g(y)dy = \theta(x)(1 - e^{-x}),$$

$$P(x) = (2\pi)^{-1/2} e^{-\frac{x^2}{2}},$$

where * represents convolution over $t$, $\varepsilon_0^T$ is the strain magnitude, $\xi$ is the spatial extent, $t_0$ is the strain formation time, $\sigma$ is the pump intensity duration, and $\theta(x)$ is the Heaviside step function. The details of how the light reflects off this strain wave to provide the amplitude and phase of the CAW are left out here, while the findings are summarized.

As shown in Figure 21b, the OC and the CC phase spectra show a very different overall phase, near 0° for OC and 150° for CC. The weighted least squares fit of the model to the phase spectra includes its spectral dependence. The fit has only the two free parameters of the interfacial strain's spatial extent ($\xi$) and formation time ($t_0$). Both panels show the best fit curves with black dashed lines. For CC, the best fit corresponds to a tensile strain with a formation time of 1.31 ± 0.03 ps and a spatial extent that converged at a 100 ± 195 nm upper bound. With a 0.9 ps formation time, which is the lower bound of the exponential fits of the emissive rise, a lower bound spatial extent of 3.4 nm is obtained. Together with fits of the CAW amplitude spectra (Fig. 21c), this gives an upper bound for the interfacial strain of 0.6% in CC. For OC, we were unable to get a reliable fit because of the spatial and temporal phases' additive property combined with the larger spread in the OC data. The best fit corresponds to a formation time that converged at the 0 ps lower bound and a spatial extent of 6 nm with standard error of $1.5\times10^4$ nm. From this, we can only conclude that the OC strain forms within the pump pulse duration.

The coherent acoustic interferometry allows for a more complete structural characterization of the hole-polarons on 0.1 % Nb $SrTiO_3$. The GHz regime of acoustic waves allows one to assign an interfacial strain to the hole-polaron coverage achieved with a 0.04 $mJ/cm^2$ excitation, or ~2% of the surface sites. That a consistent time constant exists across the electromagnetic spectrum assigns it to a free energy difference with an elevated, but common temperature of the quantum states. Further, that hole-polaron formation occurs with an interfacial strain field implicates the propagating acoustic pulse in the energy dissipation.[43, 69] On the other hand, upon subtraction of the lattice phonons in the data, one is left with a GHz mode resulting from Brillouin scattering in the electrolyte, implicating also the rotational-vibrational modes of water. The activation free energy could involve all these modes, and the time constant could be rate limited by any of one of them.

## CONCLUSIONS & OUTLOOK

This mini review covered the electronic and vibrational spectroscopy of the electron doped STO/electrolyte interface during the oxygen evolution reaction from water. The first part covered how to photo-trigger an efficient catalytic reaction by ultrafast light pulses (Part II) and the second part covered the detection of the surface bound intermediates by transient spectroscopy (Part III).

To explain the ultrafast photo-trigger and the associated methodology, Part IIA first described the Schottky diode formed at the n-STO/electrolyte interface. In many ways, this Schottky diode is a conventional one, obeying the Mott-Schottky equation, a sharp turn on of the photovoltage when sweeping the voltage, and a photovoltage at open circuit that quickly saturates with fluence. A high quantum efficiency for OER is obtained similarly for a continuous light source as the ultrafast laser and derives from a depletion width that is greater than the penetration depth of the light. On the other hand, a large Helmholtz potential drop exists on the electrolyte side that screens the electrode, covered in Part IIB. This large Helmholtz potential drop means that the band edges at the surface when equilibrated with the electrolyte or under anodic potentials on the working electrode are significantly lower than the flatband potentials. In this section, capacitor models of the interface were reviewed and the two circuit conditions, open and closed circuit, were defined. There was some attention to the effect of the electrolyte pH across the depletion and Helmholtz layers unique to semiconductors to show the importance of the inner Helmholtz layer, or what some would define as the hydration layer.

In the last section (Part IIC), the STO/electrolyte interface was reviewed for its surface characterization before and after catalysis. Prior to catalysis, characterization of the hydration layer by AP-XPS at neutral conditions shows an STO surface described by partial water dissociation, with both water and hydroxyl groups covering the surface at low doping, which is the predominant surface reviewed here. At higher doping, the surface becomes nearly fully hydroxylated, which is an interesting finding for future work. Ultrafast excitation of OER does introduce a surface dissolution and restructuring. This necessitates a sample scanning methodology which identifies a scan rate fast enough such that the effect of the degraded layer is not seen in the optical experiments. Electron microscopy determines the extent to which the dissolution of this layer can contribute to the photocurrent (below 6% at pH 13). These

assessments argued that the effect of the degradation on the optical signal would be limited to the % dissolution measured by electron microscopy.

With this setup, Part III then covers the ultrafast electronic and vibrational probes of the surface intermediates. It begins with a section (Part IIIA) that puts the electron and proton transfer from an adsorbed water species in the context of the OER reaction when it is divided into four electron and proton transfer steps. The first electron and proton transfer step is the focus of the ultrafast optical probes. This section also covers how the proton transfer can occur separately from the electron transfer at the semiconductor interface, which recalls the pH dependence of the depletion and Helmholtz layers covered in Part IIB. The next section (Part IIIB) describes the broadband visible probe of the surface intermediates by first introducing the concept of a localized hole or hole-polaron theoretically and then associating these electronic levels with mid-gap excited state absorptions and stimulated emissions seen experimentally. The optical cross-sections and visible probe depth in reflectance are delineated. The absorption and emission have distinct population dynamics that allow them to be separated in a principal component analysis. Overall, a clear dichotomy exists between the absorptive and emissive signals: the emissive signal dominates at CC, exhibits a rise time, is metastable, and saturates with laser fluence, while the absorptive signal dominates at OC, occurs within the resolution of the experiment, decays, and linearly increases with laser fluence. The challenge now is to see whether one can correlate the energies of the optical transitions to the population dynamics observed, which will require a closer collaboration with theory.

The next section, Part IIIC, covers the ultrafast mid-infrared probe of the surface intermediates. There, the assignment of a vibration to a particular electron and hole transfer intermediate, the terminal titanium oxyl ($Ti\text{-}O^{\bullet-}$), is reviewed. The evanescent wave probe of the ground state of the surface is contrasted with the excited state surface. How attenuated total reflection at the diamond interface produces this evanescent wave and its geometry with respect to the sample in the photoelectrochemical cell is described. On the excited state surface, a new vibration is isolated. That vibration is assigned to a metastable hole trapped the surface through a doping dependence, a shortened lifetime with methanol scavenging, and its population correlation with $O_2$ evolution. Then, the theoretical calculation that assigns this vibration to the terminal oxyl is described and explains its detection in p-polarized light. In the language of the visible probe of mid-gap states, the oxyl is a hole-polaron that perturbs the nearby lattice structure, such that a new dipole allowed vibration arises in the plane beneath it from otherwise dark, symmetric modes.

Finally, the last section, Part IIID, detects the hole-polarons yet in another way, which is through an interfacial strain in the continuum lattice. While the mid-infrared vibrations are of localized normal modes, a population of hole-polarons could perturb the average size of the periodic unit cell. In so doing, acoustic phonons are produced and if generated in an ultrafast manner, propagate as a wavepacket into the bulk of the sample; the acoustic wave packet then creates coherent acoustic waves (CAW) in the data through interferences of the visible probe. While the detection is again by a visible probe, it is now one that detects atomic motion. The CAW are investigated at open and closed circuit and with excitation fluence. When correlated with interfacial strain created by a high population of delocalized carriers and the excited state

absorption, the CAW have a phase of near 0°. When correlated with hole-polarons and the stimulated emission, the CAW have a phase near 150°. The phase allowed for an ultrafast formation time and sign of the strain to be assigned, again differentiating the CAW mechanism (delocalized carriers vs. hole-polarons) and the associated absorptions and emissions in the visible region.

**ACKNOWLEDGEMENTS** The experimental work involved in updating the experimental setup, taking the data, and the analysis was supported by the Director, Office of Science, Office of Basic Energy Sciences, and by the Division of Chemical Sciences, Geosciences and Biosciences of the U.S. Department of Energy at RASEI (Boulder, CO) under Contract No. DE-SC0018939.

## REFERENCES

1. Markovic, N. M., Electrocatalysis: Interfacing electrochemistry. *Nature materials* **2013,** *12* (2), 101-2.
2. Hammer, B.; Norskov, J. K., Theoretical surface science and catalysis--calculations and concepts. *Advances in Catalysis* **2004,** *45*, 71-129.
3. Kern, J.; Chatterjee, R.; Young, I. D.; Fuller, F. D.; Lassalle, L.; Ibrahim, M.; Gul, S.; Fransson, T.; Brewster, A. S.; Alonso-Mori, R.; Hussein, R.; Zhang, M.; Douthit, L.; de Lichtenberg, C.; Cheah, M. H.; Shevela, D.; Wersig, J.; Seuffert, I.; Sokaras, D.; Pastor, E.; Weninger, C.; Kroll, T.; Sierra, R. G.; Aller, P.; Butryn, A.; Orville, A. M.; Liang, M.; Batyuk, A.; Koglin, J. E.; Carbajo, S.; Boutet, S.; Moriarty, N. W.; Holton, J. M.; Dobbek, H.; Adams, P. D.; Bergmann, U.; Sauter, N. K.; Zouni, A.; Messinger, J.; Yano, J.; Yachandra, V. K., Structures of the intermediates of Kok's photosynthetic water oxidation clock. *Nature* **2018,** *563* (7731), 421-425.
4. Hammarstrom, L.; Hammes-Schiffer, S., Artificial Photosynthesis and Solar Fuels. *Accounts of Chemical Research* **2009,** *42* (12), 1859-1860.
5. Truhlar, D. G.; Garrett, B. C.; Klippenstein, S. J., Current Status of Transition-State Theory. *J. Phys. Chem.* **1996,** *100*, 12771-12800.
6. Dellago, C.; Bolhuis, P. G.; Csajka, F. S.; Chandler, D., Transition path sampling and the calculation of rate constants. *The Journal of Chemical Physics* **1998,** *108* (5), 1964-1977.
7. Cuk, T., Phenomoenology of intermediate molecular dynamics at metal-oxide interfaces. *Annual Review of Physical Chemistry* **2024,** *In-press*.
8. Zhang, M.; Frei, H., Water Oxidation Mechanisms of Metal Oxide Catalysts by Vibrational Spectroscopy of Transient Intermediates. In *Annual Review of Physical Chemistry, Vol 68*, Johnson, M. A.; Martinez, T. J., Eds. 2017; Vol. 68, pp 209-231.
9. Timoshenko, J.; Cuenya, B. R., In Situ/Operando Electrocatalyst Characterization by X-ray Absorption Spectroscopy. *Chemical Reviews* **2021,** *121* (2), 882-961.
10. Nong, H. N.; Falling, L. J.; Bergmann, A.; Klingenhof, M.; Tran, H. P.; Spori, C.; Mom, R.; Timoshenko, J.; Zichittella, G.; Knop-Gericke, A.; Piccinin, S.; Perez-Ramirez, J.; Roldan Cuenya, B.; Schlogl, R.; Strasser, P.; Teschner, D.; Jones, T. E., Key role of chemistry versus bias in electrocatalytic oxygen evolution. *Nature* **2020,** *587* (7834), 408-+.
11. Weckhuysen, B. M., Chemical Imaging of Spatial Heterogeneities in Catalytic Solids at Different Length and Time Scales. *Angew. Chem.-Int. Edit.* **2009,** *48* (27), 4910-4943.
12. Toma, F. M.; Cooper, J. K.; Kunzelmann, V.; McDowell, M. T.; Yu, J.; Larson, D. M.; Borys, N. J.; Abelyan, C.; Beeman, J. W.; Yu, K. M.; Yang, J. H.; Chen, L.; Shaner, M. R.; Spurgeon, J.; Houle, F. A.; Persson,

K. A.; Sharp, I. D., Mechanistic insights into chemical and photochemical transformations of bismuth vanadate photoanodes. *Nature Communications* **2016,** *7*.
13. Buurmans, I. L. C.; Weckhuysen, B. M., Heterogeneities of individual catalyst particles in space and time as monitored by spectroscopy. *Nat. Chem.* **2012,** *4* (11), 873-886.
14. Waegele, M. M.; Chen, X.; Herlihy, D. M.; Cuk, T., How Surface Potential Determines the Kinetics of the First Hole Transfer of Photocatalytic Water Oxidation. *Journal of the American Chemical Society* **2014,** *136* (30), 10632-10639.
15. Lyle, H.; Singh, S.; Magnano, E.; Nappini, S.; Bondino, F.; Yazdi, S.; Cuk, T., Assessing and Quantifying Thermodynamically Concomitant Degradation during Oxygen Evolution from Water on SrTiO3. *ACS Catalysis* **2023,** *13* (12), 8206-8218.
16. Courter, C.; Stewart, J.; Cuk, T., Moderate Electron Doping Assists in Dissociating Water on a Transition Metal Oxide Surface (n-SrTiO3). *The Journal of Physical Chemistry C* **2023,** *127* (10), 4905-4916.
17. Sharma, S. K.; Pavithra, D.; Sivakumar, G.; Srinivasamurthy, N.; Agrawal, B. L., Determination of solar cell diffusion capacitance and its dependence on temperature and 1 MeV electron fluence level. *Solar Energy Materials and Solar Cells* **1992,** *26* (3), 169-179.
18. Marshall, M. S. J.; Newell, D. T.; Payne, D. J.; Egdell, R. G.; Castell, M. R., Atomic and electronic surface structures of dopants in oxides: STM and XPS of Nb- and La-doped SrTiO3(001). *Physical Review B* **2011,** *83* (3).
19. Frederikse, H. P. R.; Thurber, W. R.; Hosler, W. R., Electronic Transport in Strontium Titanate. *Physical Review* **1964,** *134* (2A), A442-A445.
20. Xu, Y.; Schoonen, M. A. A., The absolute energy positions of conduction and valence bands of selected semiconducting minerals. *American Mineralogist* **2000,** *85* (3-4), 543-556.
21. De Gryse, R., Gomes, W. P., Cardon, F., and Vennik, J., On the interpretation of Mott-Schottky Plots Determined at Semiconductor/Electrolyte Systems. *J. Electrochem. Soc.* **1975,** *122*, 711.
22. Sundararaman, R.; Letchworth-Weaver, K.; Schwarz, K. A., Improving accuracy of electrochemical capacitance and solvation energetics in first-principles calculations. *The Journal of Chemical Physics* **2018,** *148* (14), 144105.
23. Cooper, G.; Turner, J. A.; Nozik, A. J., Mott-Schottky Plots and Flatband Potentials for Single Crystal Rutile Electrodes. *Journal of The Electrochemical Society* **1982,** *129* (9), 1973.
24. Rossmeisl, J.; Qu, Z. W.; Zhu, H.; Kroes, G. J.; Nørskov, J. K., Electrolysis of water on oxide surfaces. *Journal of Electroanalytical Chemistry* **2007,** *607* (1-2), 83-89.
25. Li, J.-Q.; Meng, L.; Sprik, M.; Cheng, J., Thermodynamic Investigation of Proton/Electron Interplay on the Pourbaix Diagram at the TiO2/Electrolyte Interface. *The Journal of Physical Chemistry C* **2020,** *124* (35), 19003-19014.
26. I. Vinogradov; S. Singh; H. Lyle; A. Mandal*; J. Rossmeisl; Cuk*, T., Free energy difference to create the M-OH* intermediate of the oxygen evolution reaction by time-resolved optical spectroscopy. *Nature Materials, in-press* **2021**.
27. I. Vinogradov; S. Singh; H. Lyle; A. Mandal*; J. Rossmeisl; Cuk*, T., Free energy difference to create the M-OH* intermediate of the oxygen evolution reaction by time-resolved optical spectroscopy. *Nature Materials* **2022,** *21*, 88-94.
28. Newberg, J. T.; Starr, D. E.; Yamamoto, S.; Kaya, S.; Kendelewicz, T.; Mysak, E. R.; Porsgaard, S.; Salmeron, M. B.; Brown, G. E.; Nilsson, A.; Bluhm, H., Formation of hydroxyl and water layers on MgO films studied with ambient pressure XPS. *Surf. Sci.* **2011,** *605* (1-2), 89-94.
29. Ketteler, G.; Yamamoto, S.; Bluhm, H.; Andersson, K.; Starr, D. E.; Ogletree, D. F.; Ogasawara, H.; Nilsson, A.; Salmeron, M., The nature of water nucleation sites on TiO2(110) surfaces revealed by ambient pressure X-ray photoelectron spectroscopy. *J. Phys. Chem. C* **2007,** *111* (23), 8278-8282.
30. Chambers, S. A.; Droubay, T. C.; Capan, C.; Sun, G. Y., Unintentional F doping of SrTiO3(001) etched in HF acid-structure and electronic properties. *Surf. Sci.* **2012,** *606* (3), 554-558.

31. Kawasaki, M.; Takahashi, K.; Maeda, T.; Tsuchiya, R.; Shinohara, M.; Ishiyama, O.; Yonezawa, T.; Yoshimoto, M.; Koinuma, H., Atomic Control of the SrTiO<sub>3</sub> Crystal Surface. *Science* **1994,** *266* (5190), 1540-1542.
32. Sokolović, I.; Franceschi, G.; Wang, Z.; Xu, J.; Pavelec, J.; Riva, M.; Schmid, M.; Diebold, U.; Setvín, M., Quest for a pristine unreconstructed ${\mathrm{SrTiO}}_{3}(001)$ surface: An atomically resolved study via noncontact atomic force microscopy. *Physical Review B* **2021,** *103* (24), L241406.
33. Binninger, T.; Mohamed, R.; Waltar, K.; Fabbri, E.; Levecque, P.; Kötz, R.; Schmidt, T. J., Thermodynamic explanation of the universal correlation between oxygen evolution activity and corrosion of oxide catalysts. *Scientific Reports* **2015,** *5* (1), 12167.
34. Jonas, D. M., Two-Dimensional Femtosecond Spectroscopy. *Annual Review of Physical Chemistry* **2003,** *54* (1), 425-463.
35. Bredenbeck, J.; Helbing, J.; Kolano, C.; Hamm, P., Ultrafast 2D-IR Spectroscopy of transient species. *Chemphyschem* **2007,** *8* (12), 1747-1756.
36. Fayer, M. D., Dynamics of Water Interacting with Interfaces, Molecules, and Ions. *Accounts of Chemical Research* **2012,** *45* (1), 3-14.
37. Lyle, H.; Singh, S.; Paolino, M.; Vinogradov, I.; Cuk, T., The electron-transfer intermediates of the oxygen evolution reaction (OER) as polarons by in situ spectroscopy. *Physical Chemistry Chemical Physics* **2021,** *23* (44), 24984-25002.
38. Chen, X.; Choing, S. N.; Aschaffenburg, D. J.; Pemmaraju, C. D.; Prendergast, D.; Cuk, T., The formation time of Ti-O• and Ti-O•-Ti radicals at the n-SrTiO3/aqueous interface during photocatalytic water oxidation. *Journal of the American Chemical Society* **2017,** *139*, 1830-1841.
39. Herlihy, D. M.; Waegele, M. M.; Chen, X.; Pemmaraju, C. D.; Prendergast, D.; Cuk, T., Detecting the oxyl radical of photocatalytic water oxidation at an n-SrTiO3/aqueous interface through its subsurface vibration. *Nat Chem* **2016,** *8* (6), 549-55.
40. S. Singh, H. L., L. D'Amario, E. Magnano, I. Vinogradov, & T. Cuk, Coherent acoustic interferometry during the photo-driven oxygen evolution reaction associates strain fields with the reactive oxygen intermediate (Ti-OH*). *J. Am. Chem. Soc.* **2021,** *143*, 15984.
41. Zandi, O.; Hamann, T. W., Determination of photoelectrochemical water oxidation intermediates on haematite electrode surfaces using operando infrared spectroscopy. *Nat Chem* **2016,** *8* (8), 778-83.
42. Lyle, H.; Singh, S.; Paolino, M.; Vinogradov, I.; Cuk, T., The electron-transfer intermediates of the oxygen evolution reaction (OER) as polarons by in situ spectroscopy. *Physical Chemistry Chemical Physics*.
43. Brown, D. W.; Lindenberg, K.; West, B. J., On the dynamics of polaron formation in a deformable medium. *The Journal of Chemical Physics* **1986,** *84* (3), 1574-1582.
44. Deskins, N. A.; Dupuis, M., Electron transport via polaron hopping in bulk TiO2: A density functional theory characterization. *Physical Review B* **2007,** *75* (19), 10.
45. Janotti, A.; Varley, J. B.; Choi, M.; Van de Walle, C. G., Vacancies and small polarons in $SrTiO_3$. *Phys. Rev. B* **2014,** *90* (8), 085202.
46. Reticcioli, M.; Setvin, M.; Schmid, M.; Diebold, U.; Franchini, C., Formation and dynamics of small polarons on the rutile ${\mathrm{TiO}}_{2}$(110) surface. *Physical Review B* **2018,** *98* (4), 045306.
47. Schirmer, O. F., O−bound small polarons in oxide materials. *Journal of Physics: Condensed Matter* **2006,** *18* (43), R667-R704.
48. Cheng, J.; VandeVondele, J.; Sprik, M., Identifying Trapped Electronic Holes at the Aqueous TiO2 Interface. *J. Phys. Chem. C* **2014,** *118* (10), 5437-5444.
49. McIntyre, J. D. E. a. A., D.E., Differential Reflection Spectroscopy of Very Thin Surface Films. *Surf. Sci.* **1972,** *24*, 417-434.
50. Sabbah, A. J.; Riffe, D. M., Femtosecond pump-probe reflectivity study of silicon carrier dynamics. *Physical Review B* **2002,** *66* (16), 165217.

51. Mochizuki, S.; Fujishiro, F.; Minami, S., Photoluminescence and reversible photo-induced spectral change of SrTiO3. *Journal of Physics: Condensed Matter* **2005,** *17* (6), 923-948.
52. Rubano, A.; Paparo, D.; Granozio, F. M.; Uccio, U.; Marrucci, L., Blue luminescence of SrTiO3 under intense optical excitation. *Journal of Applied Physics* **2009,** *106*, 103515.
53. Austin, I. G.; Mott, N. F., Polarons in crystalline and non-crystalline materials. *Advances in Physics* **2001,** *50* (7), 757-812.
54. Yamada, Y.; Yasuda, H.; Tayagaki, T.; Kanemitsu, Y., Photocarrier recombination dynamics in highly excited SrTiO3 studied by transient absorption and photoluminescence spectroscopy. *Applied Physics Letters* **2009,** *95* (12), 121112.
55. Fano, U., *Physical Review* **1961,** *124*, 1866.
56. Fischer, B.; Bäuerle, D.; Buckel, W. J., Surface polaritons in KTaO3 and SrTiO3. *Solid State Communications* **1974,** *14* (3), 291-294.
57. Lee, H. N.; Seo, S. S. A.; Noh, T. W., Infrared spectroscopy of CaTiO<sub>3</sub>, SrTiO<sub>3</sub>, BaTiO<sub>3</sub>, Ba<sub>0.5</sub>Sr<sub>0.5</sub>TiO<sub>3</sub> thin films, and (BaTiO<sub>3</sub>)<sub>5</sub>/(SrTiO<sub>3</sub>)<sub>5</sub> superlattice grown on SrRuO<sub>3</sub>/SrTiO<sub>3</sub>(001) substrates. **2005,** *486*.
58. Milosevic, M., *Internal Reflection and ATR Spectroscopy*. Wiley: 2012.
59. Gervais, F. o.; Servoin, J.-L.; Baratoff, A.; Bednorz, J. G.; Binnig, G., Temperature dependence of plasmons in Nb-doped ${\mathrm{SrTiO}}_{3}$. *Physical Review B* **1993,** *47* (13), 8187-8194.
60. Giguère, P. A.; Harvey, K. B., ON THE INFRARED ABSORPTION OF WATER AND HEAVY WATER IN CONDENSED STATES. *Canadian Journal of Chemistry* **1956,** *34* (6), 798-808.
61. Giustino, F.; Pasquarello, A., Infrared Spectra at Surfaces and Interfaces from First Principles: Evolution of the Spectra across the $\mathrm{Si}(100)\mathrm{\text{\ensuremath{-}}}{\mathrm{SiO}}_{2}$ Interface. *Physical Review Letters* **2005,** *95* (18), 187402.
62. Pollock, K. L.; Doan, H. Q.; Rustagi, A.; Stanton, C. J.; Cuk, T., Detecting the Photoexcited Carrier Distribution Across GaAs/Transition Metal Oxide Interfaces by Coherent Longitudinal Acoustic Phonons. *Journal of Physical Chemistry Letters* **2017,** *8* (5), 922-928.
63. Thomsen, C.; Grahn, H. T.; Maris, H. J.; Tauc, J., Surface generation and detection of phonons by picosecond light pulses. *Physical review. B, Condensed matter* **1986,** *34* (6), 4129-4138.
64. Brivio, S.; Polli, D.; Crespi, A.; Osellame, R.; Cerullo, G.; Bertacco, R., Observation of anomalous acoustic phonon dispersion in SrTiO3 by broadband stimulated Brillouin scattering. *Applied Physics Letters* **2011,** *98* (21), 211907.
65. Lu, Y.; Jia, D.; Gao, F.; Chen, Z.; Hu, T., First-principles study on the elastic properties of Sr–Ti–O ceramics. *Solid State Communications* **2014,** *182*, 43-46.
66. Pollock, K. L.; Doan, H. Q.; Rustagi, A.; Stanton, C. J.; Cuk, T., Detecting the Photoexcited Carrier Distribution Across GaAs/Transition Metal Oxide Interfaces by Coherent Longitudinal Acoustic Phonons. *J. Phys. Chem. Lett.* **2017,** *8* (5), 922-928.
67. Thomsen, C.; Grahn, H. T.; Maris, H. J.; Tauc, J., Picosecond interferometric technique for study of phonons in the brillouin frequency range. *Optics Communications* **1986,** *60* (1), 55-58.
68. Babilotte, P.; Ruello, P.; Pezeril, T.; Vaudel, G.; Mounier, D.; Breteau, J.-M.; Gusev, V., Transition from piezoelectric to deformation potential mechanism of hypersound photogeneration in n-doped GaAs semiconductors. *Journal of Applied Physics* **2011,** *109* (6), 064909.
69. Morrissey, F. X.; Dexheimer, S. L., Coherent acoustic phonon generation in exciton self-trapping. *Physical Review B* **2010,** *81* (9), 094302.